RETROFIT55

Ref. Ares(2024)7452626 - 21/10/2024

Funded by the European Union

Horizon Europe programme, grant agreement No. 101096068

RETROFIT SOLUTIONS TO ACHIEVE 55% GHG REDUCTION BY 2030

System design to deliver maximum drag reduction by PALS

WP 5 – Air Lubrication System
Task 5.1 – Determine the complete system design and Layout
D 5.1 – System design to deliver maximum drag reduction by PALS
Partners involved: LJMU, FSYS, ARM, CNR
Authors: Andrew Spiteri, Hannes Rench, Alex Routledge, Massimo Falchi, Emanuele Spinosa, Alesandro Iafrati, David Hitchmough, Onur Yuksel, Eddie Blanco Davis, Jin Wang, Stefan Harries, Roger Armson.

Project details

Project Title	RETROFIT SOLUTIONS TO ACHIEVE 55% GHG REDUCTION BY 2030
Project Type	Innovation Action
Project Acronym	RETROFIT55
Grant Agreement No.	101096068
Duration	36 M
Project Start Date	01/01/2023

Deliverable information

Status (F: final; D: draft; RD: revised draft)	F 20/10/2024
Planned delivery date	31/06/2024
Actual delivery date	20/10/2024
• **Dissemination level:** PU – Public, fully open, e.g. web (Deliverables flagged as public will be automatically published in CORDIS project's page) • SEN – Sensitive, limited under the conditions of the Grant Agreement • Classified R-UE/EU-R – EU RESTRICTED under the Commission Decision No2015/444 • Classified C-UE/EU-C – EU CONFIDENTIAL under the Commission Decision No2015/444 • Classified S-UE/EU-S – EU SECRET under the Commission Decision No2015/444	PU
Type: Report, Website, Other, Ethics	Report

Document history

Version	Date	Created/Amended by	Changes
01	02/07/2024	Andrew Spiteri (LJMU)	First Draft
02	20/09/2024	Emanuele Spinosa (CNR)	Specifications
03	22/09/2024	Alex Routledge (ARM)	Specifications
04	03/10/2024	Andrew Spiteri (LJMU)	New version including comments and specification
05	07/10/2024	Emanuele Spinosa (CNR)	Revision
	20/10/2024	Alessandro Iafrati (CNR)	Final version

Quality check review

Reviewer (s)	Main changes / Actions
Emanuele Spinosa (CNR)	Technical comments and specification
Alex Routledge (ARM)	Technical comments and specification
Cecilia Leotardi (CNR)	Minor technical review and thorough editorial review.
Cecilia Leotardi and Alessandro Iafrati (CNR)	Final review of contents and submission to EC.

Table of Contents

List of Tables

List of Figures

Abbreviations

ALS	Air Lubrication Systems
ARM	Armada Technologies
BDR	Bubble Drag Reduction
BL	Boundary Layer
CF	Co-efficient of Friction
CO_2	Carbon Dioxide
DNS	Direct Numerical Simulations
Fr	Froude Number
Fd	Froude number for Depth
EU	European Union
HMI	Human Machin Interface
IMO	International Maritime Organization
MBDR	Micro Bubble Drag Reduction
PALS	Passive Air Lubrication System
PIV	Particle Image Velocimetry
PLC	Programmable Logic Controller
NO_x	Nitrogen Oxides
SO_x	Sulphur Oxides
Re	Reynolds Number
S_w	Wetted surface area
TBL	Turbulent Boundary Layer
TKE	Turbulent Kinetic Energy
WMF	World's Merchant Fleet

Executive Summary

This report presents the design and application of Passive Air Lubrication Systems (PALS) for ships. PALS aims to create a lubricating air layer that reduces friction at the hull surface, improving fuel efficiency and reducing emissions. The document acknowledges the growing importance of regulations aimed at curbing maritime emissions: stringent regulations from the International Maritime Organization (IMO) drive the adoption of energy-efficient technologies like PALS. The document highlights how PALS offers a viable solution for ship operators seeking to comply with these regulations while improving operational efficiency.

This report provides an in-depth analysis of the operational mechanics of PALS, detailing how these systems exploit the forward motion of a ship to generate and distribute air bubbles beneath the hull. The PALS system developed by ARMADA Technologies will produce a mixture of air and water, which will be injected beneath the hull at specific points using custom-designed injectors. This document analyses the impact of critical variables on the drag reduction effectiveness of the PALS, including air and water flow rates, air-water volume ratio, and hydrostatic pressure on the hull.

This report's main objective is to provide the design and system layout for the Passive Air Lubrication System to be installed in the scale model to be tested in the main towing tank at the CNR-INM. The system will be installed on two ship hulls for testing. The system operates on a similar principle to the full-scale version, which will be outlined in the project's subsequent deliverables. The results and methodology (in particular the optimisation techniques) described in this deliverable will provide important insights for the design of the full-scale system.

The system design is achieved using computational fluid dynamics (CFD) analyses, with experimental data from previous studies at low technology readiness level (TRL) used to support this. Optimisation techniques are also employed to determine the shape and distribution of the injectors on the hull surface. The resulting numerical analysis will also provide the operating conditions of the system.

To achieve these conditions, ARMADA, with the support of the external provider ECOCHLOR, has developed a bespoke experimental rig which generates the air-bubble mixture using Venturi tubes. Water is fed in by using a pump, while air is fed in by using a compressor. Water flows through the Venturi nozzles at the required flow rate, while air is injected into the Venturi throat. To regulate the desired air and water flow rates at the inlets of the Venturi bubble generator, a series of servo-valves, operated by a dedicated feedback control system, have been installed in the rig. This control is achieved by using the flow rates read by a series of flow meters, both for the air and the water lines.

The present deliverable additionally delineates the planned investigations for the assessment of the efficacy of the PALS. As previously stated, the testing is conducted on two distinct vessels. This report describes the methodology employed in the resistance tests and provides detailed baseline results for the hulls in which the PALS are not in operation.

Overall, this report combines theoretical analysis, testing data, and CFD simulations to provide valuable insights into the design and implementation of PALS. This knowledge can be used to optimize PALS performance and maximize drag reduction for improved ship efficiency, reduced emissions, and compliance with evolving environmental regulations.

1 The Passive Air Lubrication System

The World's Merchant Fleet (WMF), with 58,000 ships, is responsible for 3% of global GHG emissions. As a country, it would be the sixth largest polluter. WMF is under massive legislative, economic, and commercial pressure to reduce emissions. WMF adoption of Zero-Carbon fuels will take several decades, cost over $1 trillion, and deliver significantly less energy/tonne vs. hydrocarbons.

Monitored waterborne Carbon Dioxide (CO_2) emission in Europe indicate that shipping releases 144.6 million tons, and inland waterway transport in the European Union (EU) results in around 3.8 million tons of CO_2 emissions per year. Furthermore, shipping is responsible for 24% of the EU's Nitrogen oxides (NO_x) and Sulphur oxides (SO_x) emissions, with very high amounts found in coastal and port areas. With the current regulations, after 2030, NO_x emissions from the maritime industry are expected to exceed the EU's land-based sources [1].

Air lubrication systems (ALS) are a technology that can be used to reduce drag on ships, improving fuel efficiency and reducing the environmental impact. It works by using a system of air blowers and nozzles to blow a thin layer of air bubbles underneath the ship's hull, i.e. between the hull and the water. This air bubble layer acts as a lubricant, reducing the friction between the ship and the water and modifying the turbulence in the boundary layer (BL), thereby reducing the overall ship drag. There are several different types of air lubrication systems, including surface effect air lubrication, submerged air lubrication, and hybrid air lubrication. Each system has unique advantages and disadvantages; the most suitable option for a particular ship depends on various factors.

The RETROFIT55 partner Armada Technologies (ARM) has developed an innovative Passive Air Lubrication System (PALS) to reduce drag, fuel consumption, and associated polluting emissions. This technology reduces today's operational spending and will enable the extensive deployment of zero-carbon fuel in the future. The working principle of the ARMADA lubrication system is illustrated in Figure 1. As the ship moves forward, seawater enters the ship through a series of inlet transition pieces (the number varies depending on the application). The water transits through a low-pressure region (inline Venturi subsystem), creating a net air suction from deck level. Subsequently, a precise mixture of air and water is delivered downstream via an outlet transition piece back to the vessel BL layer for optimal drag reduction performance.

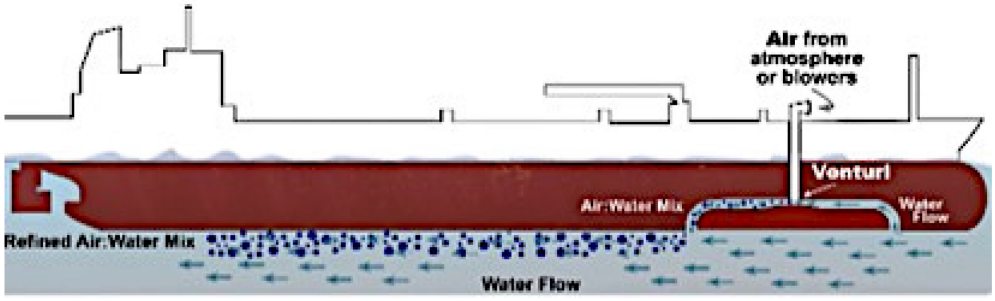

Figure 1: PALS Operation Principles

The Armada's PALS operating method is based on the Bernoulli principle and can be considered a naturally aspirated alternative to the active ALS currently on the market. The ship's forward motion is exploited to create a precise pressure differential between the geometrically refined inlet and outlet transition pieces. This pressure differential develops the net driving force to 'power' the system. An injector (Venturi) and a diffuser sit between the inlet and outlet transition pieces. The unique design

of these sub-components allows for developing a refined air-water ratio and a superior level of control of bubble size and homogeneity.

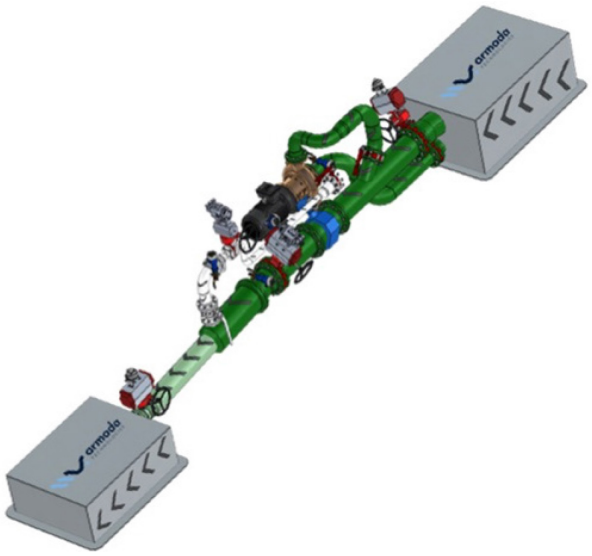

Figure 2: Isometric view of Armada's PALS

The system is supported by a PALS performance control system with integrated machine learning capability, which is designed with logic to adjust the system setpoints to the prevailing ship operating conditions. An isometric view of one of the PALS units, also known as pods, is shown in Figure 2.

The system can be monitored and controlled from one on board duplicate Human Machine Interface (HMI) panel. The HMI screens enable users to interact with the system while it operates, during system commissioning, or testing.

The PALS is designed to be a plug-and-play solution, requiring minimal human intervention. At any point, the PALS will function in one of the several predefined operating modes. A PALS functional description and control philosophy has been developed, underpinning the Programmable Logic Controller (PLC) operation. The PLC provides the monitoring and control function of the system and ensures system set points are optimal for the prevailing vessel operating condition. The PLC will control the general isolation and flow control to ensure that the mass flow and pressure settings are acceptable for the optimal operation of the ejectors. The PLC will take inputs from pressure and flow-indicating transmitters within the system and couple this with general ship information (e.g., speed, draft, global ship dynamics) to ensure successful start-up/shut-down sequencing and make necessary system adjustments in real time.

The PLC continuously captures data from all the valves and instruments, generating operational logs of each journey. This allows for analysis and performance improvement over time. These operational logs can be easily exported and sent to the technology providers for processing in our bespoke machine learning software, where assessment may lead to small changes to improve the overall system performance.

2 Working principle of the Air Lubrication Systems

The mechanism of drag reduction can be illustrated by the following equation

$$D = 0.5\, C_f\, \rho U^2 S_w \tag{1}$$

where D is the frictional drag, C_f is the coefficient of friction, ρ is the density, U is the ship velocity and S_w is the wetted surface area. The coefficient of friction is a dimensionless number that quantifies the drag force exerted by a fluid on a surface due to viscous shear stress, which, if the Reynolds decomposition of the velocity field is introduced, can be expressed as

$$\tau_w = \nu \frac{\partial u}{\partial y} - \rho U'V' \tag{2}$$

where τ_w is the wall shear stress, ν is the kinematic viscosity, y is the wall distance, u is the velocity and $\rho U'V'$ are the Reynold's stress term. Wall shear stress occurs at the surface of a vessel. It is the force per unit area exerted on the wall of the vessel by the fluid or gas flowing next to it. In the case of ships, wall shear stress is typically caused by the water flow around the hull of the vessel, as it moves through the water. Factors that can affect wall shear stress on a ship include the shape and size of the hull, the speed of the vessel, and the characteristics of the water in which the ship is operating.

With the introduction of bubbles into the BL the wetted surface area, density, and the velocity of the fluid next to the BL will reduce. As the density and dynamic viscosity decrease, the wall shear stress value drops as well, leading to a drop in the drag [2]. The friction coefficient C_f can be calculated as

$$C_f = \frac{\tau_w}{0.5\, \rho\, U^2} \tag{3}$$

Therefore, it can be assumed that the reduction in drag is due to:

- Reduction in the "effective" density
- Modification of the turbulent BL (e.g. changes in $\frac{\partial u}{\partial y}$ or in the Reynolds stress term $\rho U'V'$)
- Reduction in viscosity.

Numerous studies have been carried out to measure the resultant drag force reduction. In [3] it is observed that with microbubbles the drag can decrease by up to 70 %, whilst in [4] it is found that using a bubble volume fraction greater than 4 % can lead to a drag reduction of up to 40 %. A study conducted in [5] indicated that the drag reduction is due to at least three mechanisms, these being:

- The initial injection of the micro bubbles
- The density effect
- The effect that bubbles have on the liquid turbulence.

In [3] it is reported that increased microbubble concentration reduces the Reynolds stresses and turbulence production in the BL whereas in [2] it is stated that the microbubble drag reduction (MBDR) is due to the alteration of the viscosity density of the fluid in the BL. These changes reduce the Reynolds stresses, which minimises shear stress. The study in [6] indicates that introducing air

bubbles into the laminar region of the boundary layer minimizes the formation and development of turbulence.

The resultant net shear stress is reduced since the bubbles have lower shear stress than most solids. In some work, it is thought that the introduction of air reduces the overall viscosity of the BL and hinders turbulence production near the hull, see [7], [8] and [9].

In [3] it is noted that the increasing amount of microbubbles within a BL is inversely proportional to the Reynolds stress. It is known that the Reynolds Stress, which indicates the level of turbulent fluctuations in a fluid flow, is responsible for the transfer of energy from large to small scales and for turbulence production. When air is introduced, the turbulence production is delayed [7].

When bubbles break up, they extract turbulence energy, therefore reducing turbulence. Turbulence energy is the amount of kinetic energy present in turbulent flow. It is measured in turbulent kinetic energy (TKE), the sum of the kinetic energy associated with the velocity fluctuations related to the Reynolds stress. TKE is generated by the action of large-scale velocity fluctuations, which are transferred to minor scales via cascading. Later, this was proven to be true by using Particle Image Velocimetry (PIV) by [10]. Additionally, it was found that the flow velocity gradient changes in the turbulent layer. This could be because bubbles migrate into vortical structures, thus disrupting them, [11], [12], and [13].

When the bubbles split, the diameter is reduced, making the bubbles smaller. When this occurs, the bubbles are pushed away from the wall due to buoyancy effects and turbulent eddies. This will result in restoring the turbulent boundary layer (TBL) and reducing the volume fraction. As the smaller bubbles escape the TBL further away from the injection point, only the larger bubbles will be left, leading to an overall reduction of volume fraction and bubble concentration, see [14]. An increase in the Reynolds number (Re) will result in a greater turbulence shearing effect and bubble breaking effect, which will in turn lead to an enhanced bubble escape. This may lead to a challenge in maintaining the presence of the injected bubbles downstream [15].

The work done by [16] shows how the coefficient of friction C_f increases further away from the injection both longitudinally and transversely. In [17] it is shown that drag reduction in the spanwise direction is not uniform, and it decreases further away from the centreline of injection. In [11] and [13] it is reported that the drag reduction effect is lost the further the drag is measured downstream. This was thought to be due to the near-wall shears in the BL.

This wall shear makes the bubbles move from the wall's surface, as confirmed in [18] and, therefore, the shape of the injection point is also an important parameter. In [19] the efficacy of a side wall of 10 mm height in preventing the escape of bubbles is evaluated and its effectiveness was proved.

As demonstrated in this brief literature review, the injection of air into the boundary layer of a vessel gives rise to a multitude of complicated flow phenomena, a significant part of which remain unresolved in fluid dynamic simulations that account for real-scale conditions.

2.1 Variables Affecting Drag Reduction

From the literature available, drag reduction effect may be related with multiple mechanisms acting simultaneously. Hence a proper mathematical scaling of Bubble Drag Reduction (BDR) is yet to be achieved, e.g. [11] and [20].

The physical properties of boundary layers that are filled with microbubbles and the resultant drag reduction have been investigated for years and are still only partially understood [21]. The most

widely accepted theory is that drag reduction is achieved due to the reduction of wetted surface area. Keeping the volume fraction constant will also give different results at different Re and pressure. The parameters will affect the bubble dynamics, leading to either a drag reduction or a drag increase [22]. Once more, there is considerable ambiguity surrounding this topic, as researchers have not yet conducted a comprehensive parametric analysis.

Furthermore, several non-linear phenomena are involved, resulting in a considerable discrepancy between the findings documented in the existing literature. Table 1 shows all the variables affecting drag reduction in a bubbly flow, whilst Table 2 shows the dimensionless parameters which govern the physics of the problem, as shown in [11] and [23].

It is also important to recognise that the dynamics of a bubble of a given size are dependent on a large number of variables. This frequently results in an immediate alteration to the characteristics of the bubble, making it difficult to anticipate the future course of the phenomenon in question, see e.g. [24] and [25]. Capturing the bubbles is also difficult in experimental work, because it is difficult to predict the bubble development once they are injected.

Table 1: Performance variables of an air lubrication system

Controlled variables	
Fluid Flow Velocity	U
Air Injection Rate	Q_a
Flow rate of water in the boundary layer	Q_w
Injection ratio	$\alpha = Q_a/Q_w$
Injection Area	I_A
Injection Angle	I_{AN}
Bubble Diameter	d
Boundary layer characteristics	
Boundary Layer Thickness	δ
Turbulence Kinetic Energy	TKE
Turbulent Viscosity	μ_t
Air Layer Thickness	$\emptyset$
Environmental parameters	
Hydrostatic Pressure	P
Gravity	g
Liquid Viscosity	μ
Density Ratio	ρ
Salinity	‰
Surface Roughness of Plate	Ra

Table 2: Dimensionless parameters describing the physics of the problem

Dimensionless parameters	
Reynolds Number	Re
Froude Number	Fr
Weber Number	We
Capillary Number	Ca
Mach Number	Ma
Volume Fraction	$\propto$

2.1.1 Effect of the Volume Fraction

The influence of the volume fraction has also been discussed extensively. The **volume fraction is** a dimensionless quantity representing the ratio of the volume of a particular phase (e.g., liquid, gas, solid) to the total volume of a cell or computational element. It is a fundamental variable in multiphase flow simulations. In this context, the volume fraction is a ratio of air to water. Many researchers agree that increasing the volume fraction of air decreases drag. However, it was stated in [26] that this only holds if the fraction of air increases near the wall and [28] say that there exists a point at which, once exceeded, the addition of more air starts reducing the effect of drag reduction. For MBDR to be as efficient as can be, the air injection rate has to be optimised [29].

It can also be noted that for almost all experimentation, the higher the speed, the less the drag reduction. There seems to be a point where increasing speed reduces drag. This could be due to the fact that, as the velocity of the vessel increases, the wave making resistance component of the ship increases, reducing the viscous friction part, as reported in [2], [16], [29], [30], [31] and [32]. Turbulence also plays a significant role. As the vessel goes faster, the turbulence increases, and the bubbles are pushed out of the BL. It should be added that in most studies the injection ratio is kept the same when the velocity of the water or model is increased. Therefore, a higher velocity means that the air injection is decreased leading to a less drag reduction.

To date, there is no definitive method for estimating the air injection rate Q_a. However, it can be assessed as an indicator of boundary water flow which can be calculated by using common turbulent fluid relations [30].

The ratio of the injected flow rate (Q_a) over water flow rate (Q_w) inside of the BL is defined as:

$$\alpha = \frac{Q_a}{Q_w}. \tag{4}$$

By using the turbulent boundary theory to calculate the water flow rate

$$Q_w = U_f(\delta - \delta^*)\, B \tag{5}$$

and then [30]

$$Q_w = 0.293\ L^{0.8}\ \gamma^{0.2}\ V^{0.8}\ W \tag{6}$$

which includes the flow parameters provided in Table 3.

Table 3: Flow and plate parameters

Flow and plate parameters	
Breadth of Plate	B
Flow Velocity	U_f
Boundary Layer Thickness	δ
Kinematic Viscosity	γ
Length of Plate	L
Velocity of Plate	V
Width of Plate	W

The studies conducted by [30] and [33] show that an injection ratio of 0.4-0.6 of the boundary layer volume being filled with air resulted in the highest drag reduction affect. This can be seen in from Figure 3. However, this has only been achievable in lab tests, as filling the boundary layer of a large vessel with 40 % of air requires a large amount of air and most systems in the current market will not be able to achieve this due to design limitations.

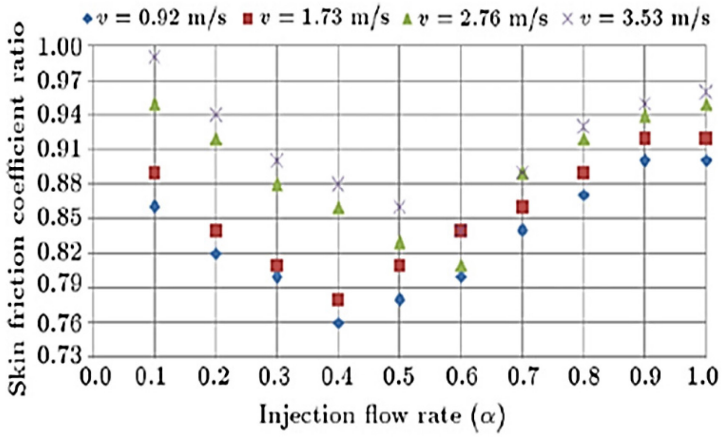

Figure 3: Skin Friction vs. Injection Rate for Four Different Velocities [30].

2.1.2 Effect of hydrostatic pressure

Hydrostatic pressure can be defined as the pressure exerted by a fluid at equilibrium at a given point within the fluid, due to the force of gravity. It increases in proportion to the fluid density and the depth measured from the free surface. As the hydrostatic pressure increases, so does its effect on air. Being air compressible, the change in depth will change the properties of the ALS and hence its drag reduction effect. In full-scale trials of on the Pacific Seagull and the M.V. Soyo, it was shown that in ballast condition the Pacific Seagull and M.V. Soyo obtained a saving of 10% and 5 % respectively whilst these savings went down to 5% and 3 %, respectively, in the fully loaded conditions.

In [34] it was discovered that for transitional air injection, i.e., starting as an air layer and ending up as a bubble and a fully developed layer, the effect of depth at slow speeds results in an increase of power needed via the compressors. In particular, it is observed that the work done by a pump to inject air at a given depth scale with the square of the ship's draft. Furthermore, the increased hydrostatic pressure makes air compressibility significant and thus a higher mass flow rate is needed to supply air at a given rate.

In [29] it was suggested that the Froude number based on the depth F_d should be calculated as follows, where U is the velocity, g is the gravity and D is the depth.

$$F_d = \frac{U}{\sqrt{gD}} \tag{7}$$

The higher the Froude number, the higher the drag reduction effect. From equation (7), it can be noted that increasing the depth (D) of the water will reduce the Froude number, hence reducing the drag reduction effect.

Furthermore, as the hydrostatic pressure increases with depth, the pressure exerted on the bubbles changes, accordingly, resulting in a corresponding alteration in bubble size and in the ratio between

the bubble layer thickness ratio to the BL thickness. Such a change is strongly influenced by the scale of the tests and it might have a strong relevance in the extrapolation of the results at full scale [12].

3 Objectives of the experimental activity

The experimental program that is being carried out in RETROFIT55 is dedicated to demonstrating, at model scale, the effectiveness of the PALS concept. The general principle regarding specific technological applications has already been validated at both the model and full scale levels. However, the system under investigation in the current project requires additional insight due to its innovative concept, which relies on a passive approach and promises to reduce power requirements and allow for a more favourable overall energy gain.

To this aim and to prove the validity of the selected PALS, as previously mentioned, two different vessels have been selected: a container and a bulk carrier. These two ships present different dimensions, displacements, and operating parameters and have been appropriately chosen to assess the performance of the current PALS for different candidate ships.

In this view, a vast experimental campaign, composed of two steps, has been designed.

1. In the first part, reported in the present document, **a baseline resistance test campaign** on the ship models in their original configuration, i.e., with no modifications on the hulls, is performed. The goal is to measure the hull overall baseline resistance, evaluate the frictional resistance, and deduce the residual resistance. These results are detailed in Section 8.
2. In the second part, which will be documented in deliverable D5.2, **the total resistance will be measured with the ALS system installed and in operation** onboard the two hulls. By comparing these results with the baseline results, the reduction in the total and frictional resistance will be estimated, assessing the effectiveness of the selected concept.

3.1.1 CNR Towing Tank

The Towing Tank “Umberto Pugliese” is a classical, free surface basin. It is 470 m long, 13.5 m wide, and has a depth of 6.5 m, see Figure 4 and Figure 5. The tank has a 50-ton towing carriage powered by 4x92 kW electric motors with Ward-Leonard control. The carriage moves on rails over the entire length of the tank, with no parts in contact with water. Depending on the model to be towed, the carriage speed can reach 12-14 m/s and is controlled with a 0.1% precision (i.e., ± 1 mm/s at 1.0 m/s).

The towing tank is used for many types of investigations such as resistance and propulsion tests for performance evaluation of surface and submersible vehicles. The tank size offers excellent capabilities for investigating large, self-propelled models of high-speed vessels (mono—or multi-hull, semi-planning and full planning craft, etc.). Equipment and methodologies for testing submarines and sailboats are available. Various unconventional marine vehicles are also designed and tested.

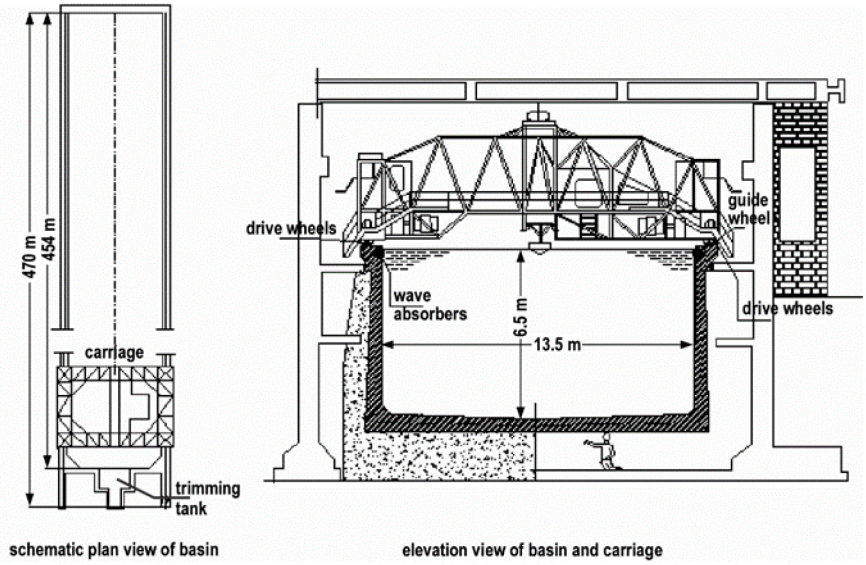

Figure 4: Sketch of the CNR-INM towing tank in plain view and section

Figure 5: Picture of the dynamometric carriage

The facility is equipped with a full range of measuring systems: force balance dynamometers, model propeller transmission dynamometers, 5-hole Pitot tube rakes for wake surveys, 1 to 6-component balance for rudders and ship models tests, fully submerged propeller dynamometer (thrust range = ± 400 N, torque range = ± 15 Nm, speed range = 60 to 3000, rpm motor power 5 kW, right and left-hand rotation, inclined operation up to ±15° in the vertical plane) for open water characterization of propellers in axial or inclined flow, 3-D optical system and inertial platform for measuring ship model motions, three-components SPIV, two-components LDV measurement systems. Further information are available at www.inm.cnr.it/labs/umberto-pugliese-towing-tank/.

3.1.2 Vessels under investigations

Two vessels will be used for the testing: the A2B vessel and the Japanese Bulk Carrier (JBC). The JBC vessel is a slower, more comprehensive ship with a deeper draft, while the A2B is faster, slender, and has a shallower draft. This allows the PALS to be tested across a range of ship conditions resulting in a better understanding of the system and a more straightforward path of optimization for different ship types and operating conditions.

The pictures of the scaled models of the A2B and JBC vessel, which will be tested in the CNR Towing Tank, are shown in Figure 6 and Figure 7, respectively. The main characteristics of the A2B and JBC model are reported in Table 4 and Table 5 , respectively.

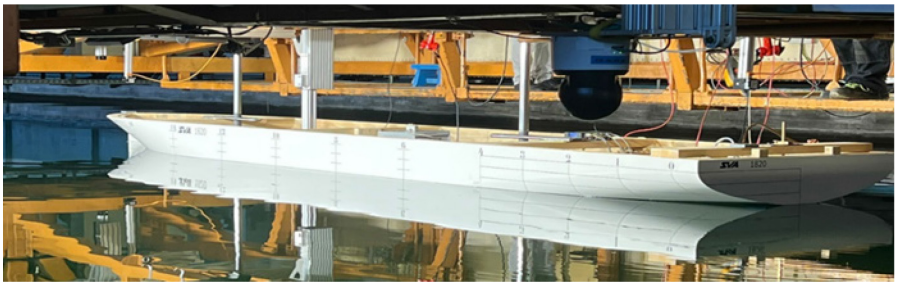

Figure 6: A2B Vessel Model

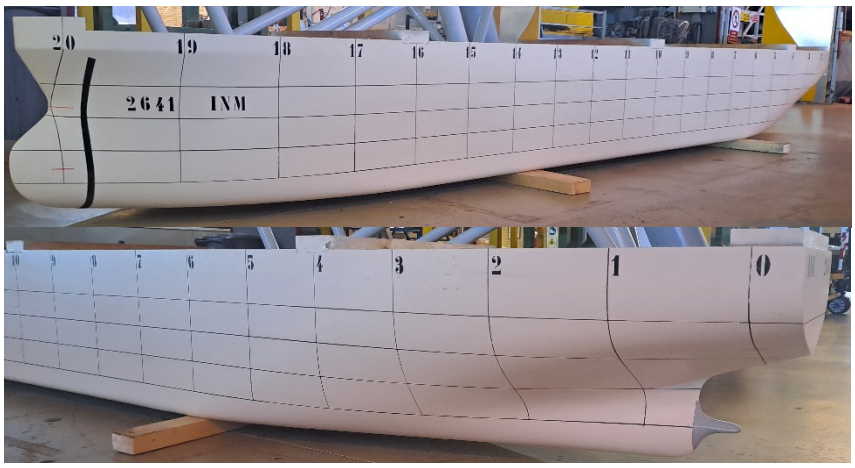

Figure 7: JBC model

Table 4: Characteristics of the A2B hull (model and full scale)

ID	Acronym	Model	Full Scale	Unit
Length Between Perpendiculars	L_{pp}	6.174	120.40	[m]
Breadth	B_{WL}	1.115	21.75	[m]
Design Draught	T	0.282	5.5	[m]
Displacement	∇	1.229	9112.8	[m^3]
Scale	λ	19.5	1	[-]

Table 5: Characteristics of JBC hull (model and full scale)

ID	Acronym	Model	Full Scale	Unit
Length Between Perpendiculars	L_{pp}	5	280	[m]
Breadth	B_{WL}	0.804	45	[m]
Design Draught	T	0.295	16.5	[m]
Displacement	∇	1.016	178369.9	[m^3]
Scale	λ	56	1	[-]

4 Design of the PALS injector shape and distribution

In order to optimise the shape of the injectors and their arrangement in the vessel, a parametric modelling approach was employed, in conjunction with a design-of-experiment methodology (see [35]). This was done with a specific focus on the towing tank tests. Due to the large difference in vessel characteristics and operating conditions, this has been carried out separately for both vessels to be tested.

In consideration of the fact that the water-air mixture is provided by an external system in the towing tank tests, the intake has been excluded from the present analysis. During the optimisation process on the full-scale PALS, the intake would be optimised separately, to maximise the pressure differential obtained within the system at a prescribed volumetric flow.

4.1 Objective Functions and CFD-Methodology

To optimise a geometry an objective function is required. In the case of an air lubrication system, the optimised quantity is the viscous resistance. Qualitative considerations on the air coverage are taken into account.

The flow and bubble distribution are simulated using a CFD approach. The simulations are run using a specialized and upgraded version of OpenFOAM®. More details are provided in [36] and [37]. In this CFD code, the Reynolds-Aaveraged Navier-Stokes (RANS) equations are solved on an unstructured grid, using the finite volume method. the pressure velocity coupling uses the PIMPLE method, a combination of the SIMPLE [38] and PISO [39] methods. Turbulent viscosity is computed using the k-ω-SST turbulence model, [40]. The free surface is captured using the Volume-of-Fluid (VoF) method [41]. The BRICS scheme, [42], is used for convective transport of the VoF-scalar, providing compressive behaviour to keep the interface sharp. The bubble dynamics is disregarded, only the presence and amount of air underneath the hull are computed by using this approach.

A significant limitation of the aforementioned methodology is that the actual bubble dynamics is not modelled but a volume-weighted averaged "mixture" of water and air is employed. Although this approach yields an accurate distribution of the bubble layer, as demonstrated in external experiments (not published), the absolute values of frictional drag remain uncertain. Nevertheless, the experiments have indicated that incorporating frictional drag as an objective function provides a useful qualitative reference for the effectiveness of air lubrication.

4.2 Optimisation of the injector shape

4.2.1 Numerical Setup

A fully parametric approach has been chosen for modelling the injector, to provide large design flexibility within the intended design space. This approach allows for the variation of all relevant angles, distances, radii, and cross-sections, with very few design variables. Figure 8 shows a generic representation of the injector shape and design space. It is worth noting that the fully parametric model would be the same for both intake and injector, but the target functions differ.

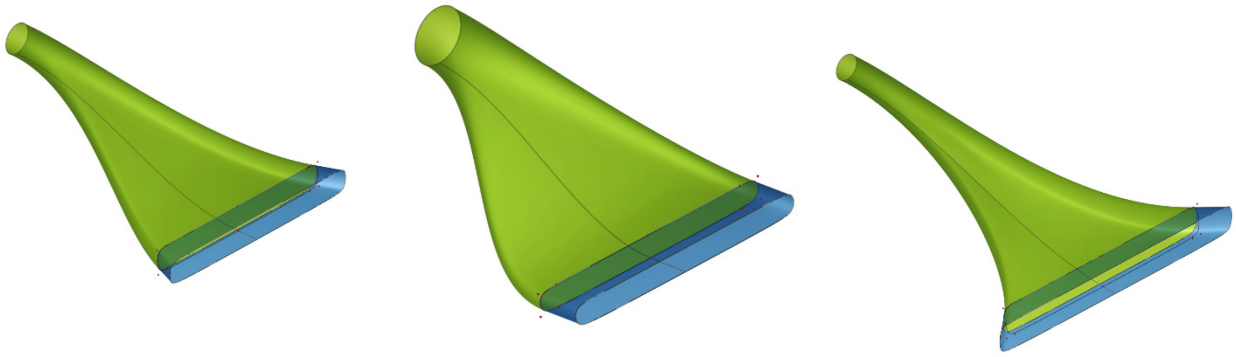

a) Baseline b) Lower extreme c) Upper extreme

Figure 8: Generic Representation of Parametric Injector Model and extremes of the design space, not to same scale

The simulations are carried out in a domain similar to the HyKaT cavitation tunnel at the Hamburg Ship Model Basin (HSVA). The objective function is evaluated on a “balance plate” downstream of the injector.

4.2.2 Optimisation Process and Results

During optimisation, the plausible design space is first evaluated to optimise the injector geometry. This is achieved using a Sobol distribution of the variables within the parameter bounds. Approximately 35 variants are required to characterise the design space properly for 6 free variables. Based on this description, a response surface (RSO) model is set up to search for actual optima. Here, another five variants were required until reaching the point of diminishing returns. The progression of the objective function during design space exploration and optimisation is shown in Figure 9.

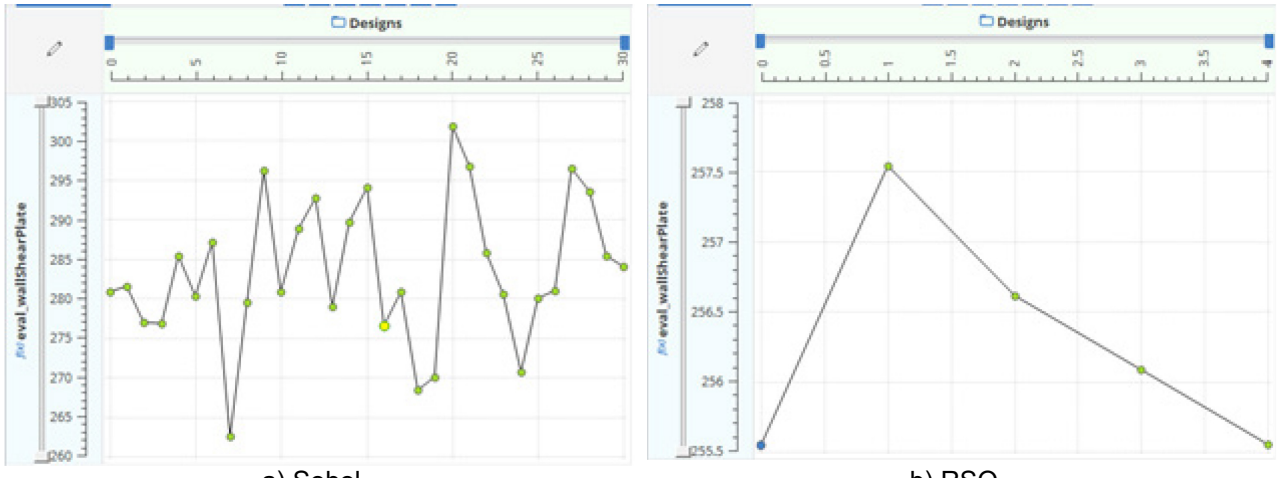

a) Sobol b) RSO

Figure 9: Progression of objective function (viscous resistance) during design space exploration and optimisation

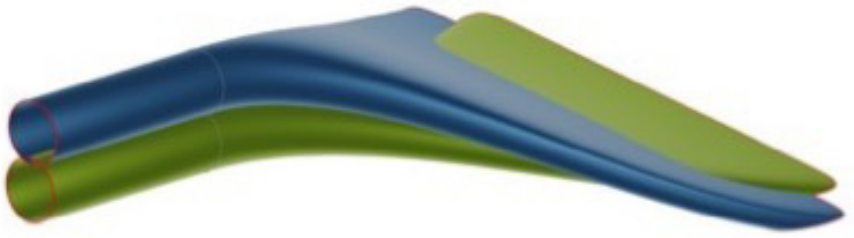

Figure 10: Optimised injector geometries for JBC (blue) and A2B (green) hulls

This exploration and optimisation process is the same for both vessels tested, but different operating conditions result in different geometries. In Figure 10 a comparison of both geometries optimised for the JBC (low speed, high draught) and A2B (higher speed, low draught) hulls is shown. The main drivers for the different shapes appear to be the different flow rates, due to compressibility, and different required injection velocity, respectively.

The effect of the injector geometry on the bubble pattern is shown in Figure 11 and Figure 12. Some unfavourable bubble patterns are shown in Figure 11. While some geometries introduce narrow but highly concentrated bubble streams (panel A), others may create oscillations due to destabilising the boundary layer (panel B), or a highly inhomogeneous distribution (panel C). Ideally, a wide-spread, stable bubble stream with sufficiently high and homogeneous concentration is sought. With the same amount of air injected, the improvement in air coverage of the balance plate from worst to best is 15%.

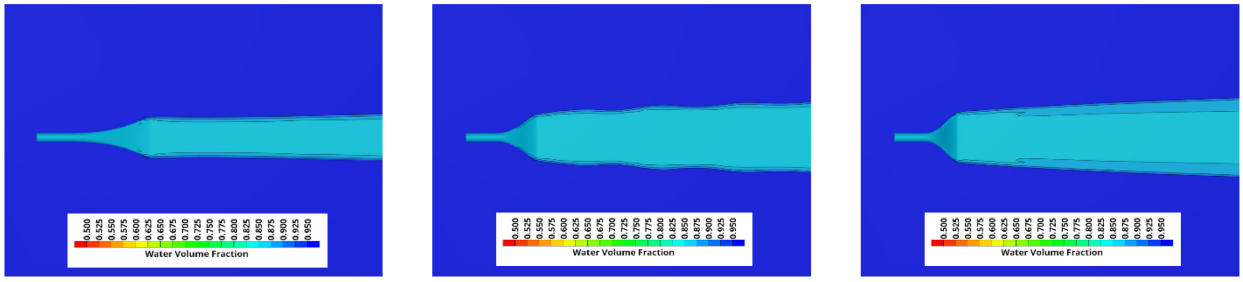

Figure 11: Volume fraction contour maps of unfavourable bubble distribution cases

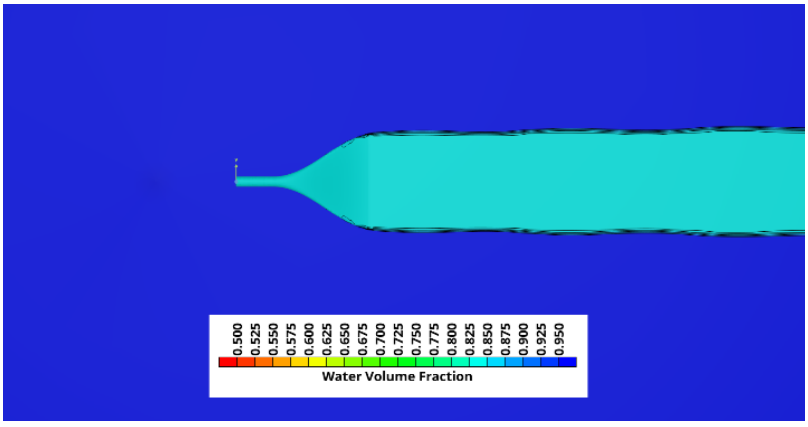

Figure 12: Volume fraction contour maps of a favourable bubble distribution case

4.3 Optimisation for the Injector arrangement

4.3.1 Numerical setup

After optimising the injector's geometry for the flow situation encountered beneath the hull, the next step is to identify an individual arrangement for each specific hull form, to maximise the benefits of the PALS. This is based on the following considerations:

1. The number of injectors per side depends on the vessel's beam and flat-of-bottom (five for the A2B, seven for the JBC).
2. All injectors with their entire length have to be installed in the flat-of-bottom.
3. The injectors must not collide.
4. Downstream systems may not be in the wake of upstream ones, to avoid air ingestion.

To ensure that points (2) to (4) are fulfilled, the positions of the injectors are defined relative to each other and to geometrical limits describing the allowable installation region.

As a consequence of the optimisation process being focused on the towing tank tests, two principal differences have emerged in comparison to the optimisation of a full-scale installation:

- while the length of the systems is taken into account during the definition of the geometrical limits and relative positions (see Figure 2 for a depiction showing the entire full-scale system) the intakes are disregarded;
- in a full-scale installation, the possible locations would be severely constrained by the vessel's structural requirements: even though the optimisation process would disregard these constraints to allow optimisation in a continuous space, the locations would be modified aposteriori to fit into the existing structure. Due to the lack of structural information (or constraints) in the considered cases, this re-arrangement has been omitted.

Figure 13 gives an overview of the flat bottom of one of the vessels investigated in this study and the initial arrangement before optimisation. The permissible region, i.e. the flat bottom, is depicted in gold colour.

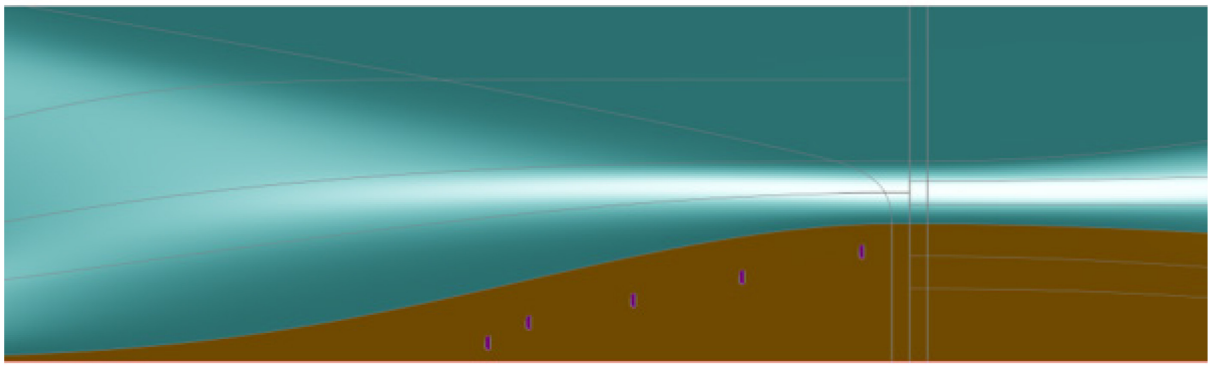

Figure 13: Close-up of initial arrangement and permissible installation region (gold)

The simulations to evaluate and provide input for the objective function for the assessment of the arrangement are run in a double-body setup, i.e., the free surface is disregarded. This is because, for this purpose, the wave pattern is assumed to have negligible effect on the flow underneath the hull.

4.3.2 Optimisation Process and Results

The optimisation approach (Sobol followed by RSO) is the same as used previously for the injector shape. Per vessel, 70 variants were used to explore the design space and 15 for the response surface-based optimisation.

4.3.2.1 A2B Hull

For the A2B hull, the installation space is severely constrained by the low block coefficient and resulting small flat-of-bottom (see Figure 13). The resulting range of installation options are given in Figure 14.

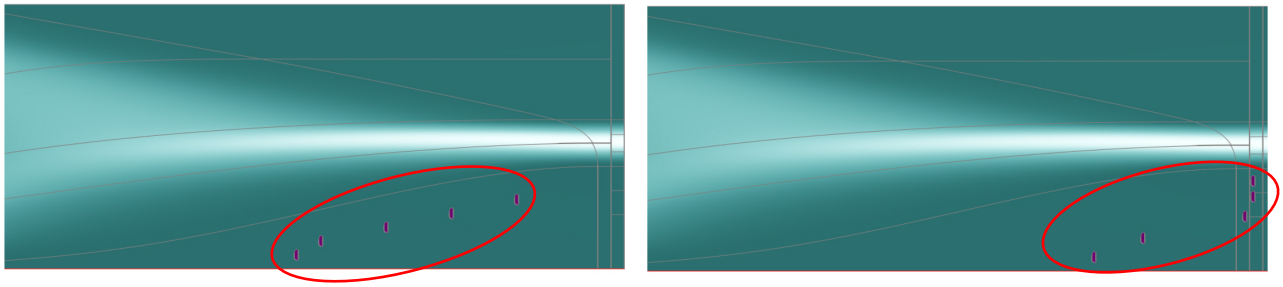

a) Foremost option b) Aftmost option

Figure 14: Injector arrangement in A2B hull

The CFD results indicate that, besides the obvious question of overall longitudinal installation, the quality of the air bubble coverage appears to be a determining factor. Further, a too-far-forward installation of the outer systems seems to lead to a loss of air due to disturbance by the forward bilge vortex.

In the context of this specific hull shape, the far-aft installation configuration illustrated in Figure 15 has the potential to negatively impact the quality of coverage. This is due to the fact that the bubbles penetrate the lower-speed, thick boundary layer region situated towards the aft portion of the hull before the air bubble sheet has had sufficient time to stabilise.

In the optimised installation (Figure 16) only the innermost systems are brought forward and inboard significantly. Even though a gap appears in the bubble carpet, the bubble coverage on the stern gondola is improved.

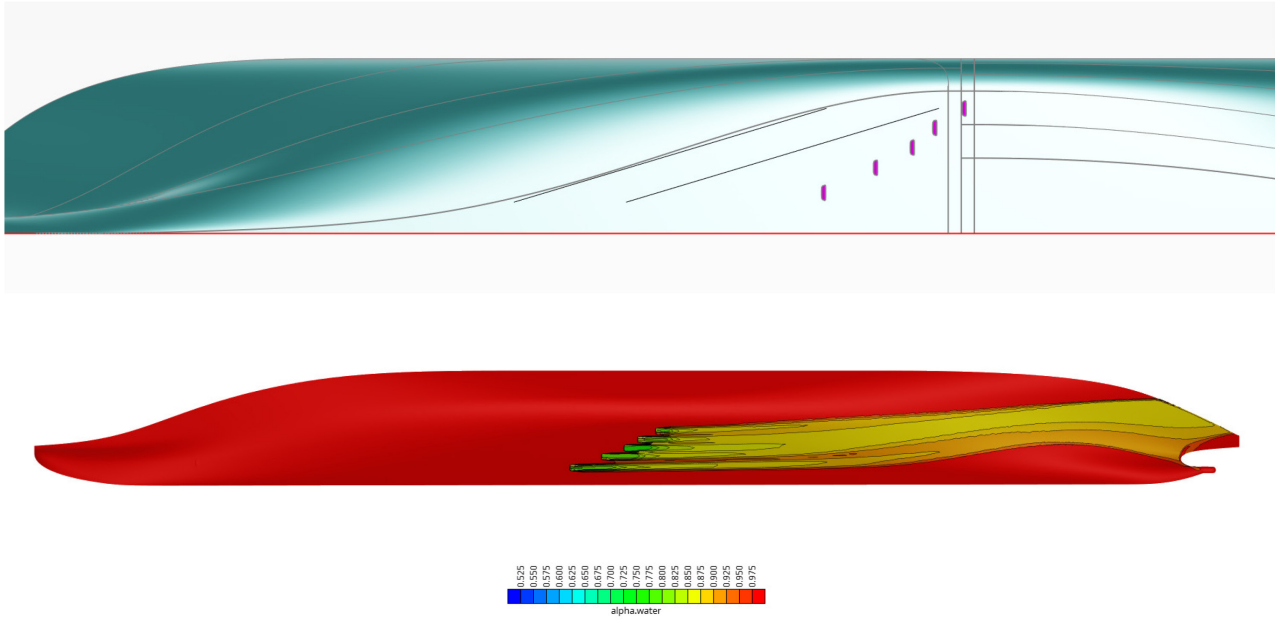

Figure 15: Far-aft PALS installation

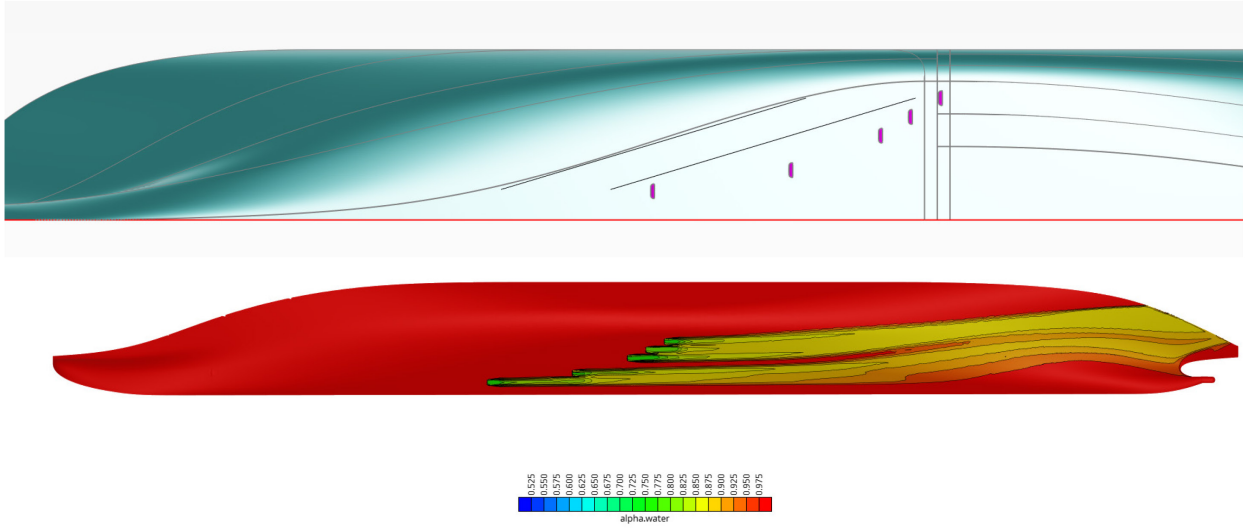

Figure 16: Optimised PALS installation

4.3.2.2 JBC Hull

Due to the ship's length, slow speed, and high block coefficient, the design space for the optimisation of the PALS installation in the JBC hull has been constrained to the region affected by the forward bilge vortex (see Figure 17).

During the investigation, it was found that the differences between the installations were below 1% of the total viscous drag. As this can be safely assumed to be within the error margin of the CFD simulations, it is not easy to draw reliable conclusions. The results seem to indicate that it is beneficial

to have a balanced distribution of the injectors over the width of the vessel while keeping them moderately forward (see Figure 18 and Figure 19).

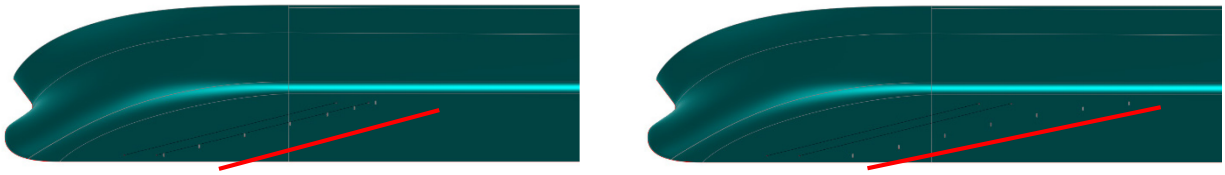

a) Foremost installation option b) Aftmost installation option

Figure 17: Injector arrangement in the JBC hull

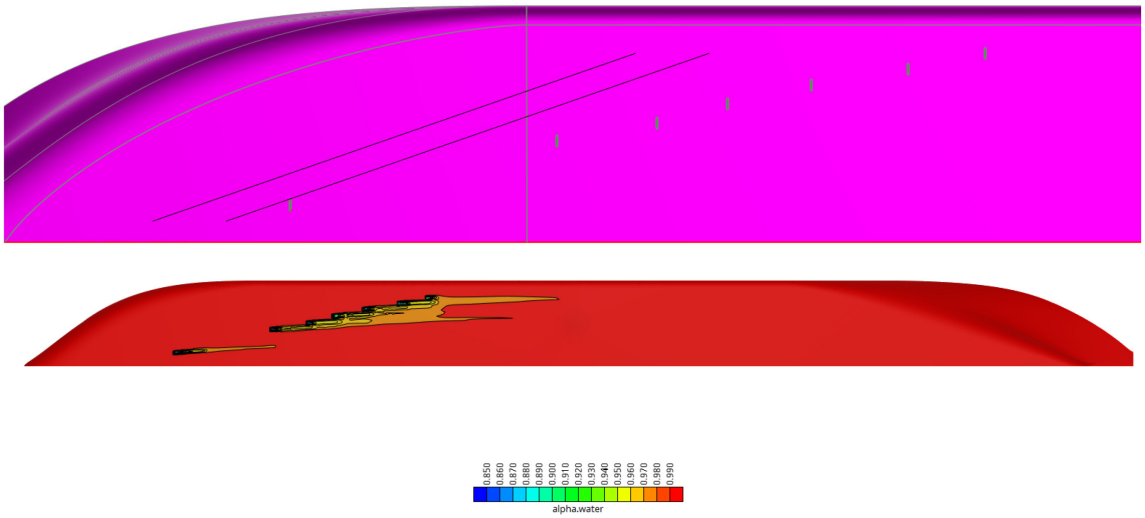

Figure 18: Variant with the highest viscous drag

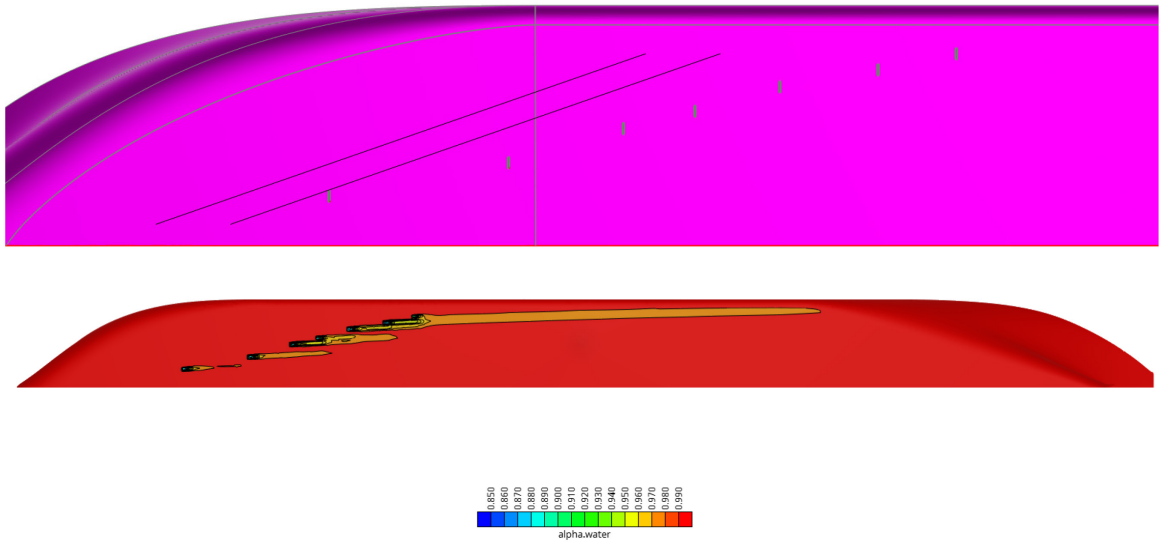

Figure 19: Variant with the lowest viscous drag

5 Definition of the Test Conditions

As specified above, the test campaign on ship models in charge of CNR-INM has been designed in two parts.

- The first phase is devoted to the **resistance characterisation of the ship models in their original configuration**. The resistance of the selected models, C_T, is measured together with the fore and aft immersions. This preliminary part is used to assess the two hulls' global characteristics and evaluate the residual resistance, C_R. This fraction of the total resistance, which depends on the Froude number only, will not be affected by the injection of the air/water mixture under the keel, allowing a baseline to calculate the amount of reduction in the frictional resistance, modified by the lubricating action. Measurements have been repeated both in bare hull and fully appended conditions for the A2B ship model, characterized by a gate rudder™ driving device, as reported below. The resistance characteristics of the JBC model have been acquired in bare hull conditions only.
- The second part of the experiments will occur after the two hulls are machined and the corresponding sets of outlets are mounted. This part of the program is devoted to checking and measuring the effectiveness of the proposed lubrication concept, performing the **measurements both in lubricated and non-lubricated conditions**. High-speed visualizations will be provided to provide a deeper insight into the development and evolution of the lubricating carpet below the keel. A high-speed camera, placed in an underwater case at a fixed station along the tank, will be employed to record its shape and stability.

For both parts, measurements are repeated for several advancing velocities to fully characterize the so-called resistance curve. For the second part, three different test regimes were identified, as below.

Investigation 1: Different hull velocities with constant flow rate. In this investigation, the set flow rate of the PALS will be tested at different velocities. The result of this will identify if the injected flow rate needs to be changed with velocity and at what point is the optimal injected flow rate concerning vessel velocity.

Investigation 2: Constant hull velocity for different ratios of total flow rate. Different injection rates will be tested for one velocity in this test regime. This will draw a relationship between the boundary layer thickness, Reynolds number, and water - air injection flow rates. This test will then be performed for several velocities. The range of this test will vary from 75% of the designed flow rate to 200% of the designed flow rate.

Investigation 3: Constant velocity and constant water injection flow rate with variable air injection rate. This will give a better understanding of the ratio of the water-to-air behaviour, as well as the relationship between injected air and the BL thickness.

Seven velocities were chosen for both vessels, as shown in Table 6 and Table 7. Some tests must be excluded from the programme of work as the specifications exceed the capabilities of the current rig system.

Table 6 Velocities to be Tested for the A2B Model

Velocity (m/s)	Froude Number
1.165	0.150
1.281	0.165

1.398	0.180
1.514	0.194
1.631	0.209
1.747	0.224
1.864	0.239

and

Table 7 Velocities to be Tested for the JBC Model

Velocity (m/s)	Froude Number
0.574	0.082
0.714	0.102
0.854	0.122
0.998	0.142
1.135	0.162
1.275	0.182
1.415	0.202
1.555	0.222
1.695	0.242

These are representative of the vessel's actual speed and Froude number which remains constant between the model and the full scale to assure that the non-dimensional wave resistance component is the same at the two scales.

The flow rates were scaled down by LJMU using the following methodology. The water flow is depth agnostic and kept constant throughout the testing while the air flow rate varies. A scaling ratio of the air to water injection rate is found to be to the power of 2.5. In fact, the outlet area has a cross-section scaling ratio to the power 2 and velocity to the power of 0.5. So, the flow rate, which is area * velocity, has a combined scaling ratio to the power of 2.5. Being the ship scaling factor indicated as λ, the scaling flow rate equation is:

$$Q_{(model)} = \frac{Q_{a,w\ (fullscale)}}{\lambda^{2.5}} \quad (8)$$

Some tests must be excluded from the programme of work as the specifications exceed the capabilities of the current rig system.

6 Bubble Generation Rig

The rig design has been developed concurrently with the development of the test matrix. Due to the significant scaling factor of the JBC, the injected flow rates are minimal. Sourcing the parts necessary to design the rig took considerable time. Table 8 shows the bill of material for the as-built rig while a few pictures of the finalised modular rig are shown in Figure 20.

Figure 20: Picture of the modular bubble generation rig

The test rig provides hull lubrication by mixing controlled water and air flow rates. A water pump and air compressor are used for the rig's supply, with the outlets delivered to the model's injectors.

The centrifugal water pump pulls water from the test basin, with the pump's outlet connected to the test rig's water inlet. Depending on test requirements, the water flow can be split for up to 14 injection lines. Flow is accurately controlled using a PLC by varying the flow control valves for each injection line (operating on a closed loop with an associated flow meter).

Air is supplied via a compressor to the test rig, set at 6 bar to protect downstream components. A singular flow control valve and flow meter accurately control the total air flow rate, supplied to two manifolds positioned on the model ship. The manifolds incorporate manual flow control valves for each air injection line, to allow tuning, ensuring an even distribution of air to each injection point.

Finally, water and air are mixed in a small **Venturi nozzle**, in which water flows though the inlet and air is entrained on the suction side. The Venturi nozzle acts as a **bubble generator**, in which when large bubble enter at the throat break down to much smaller bubbles due turbulence effects and the flow acceleration in the diverging part. The Venturi's outlet is connected to the injector piece via a short length of tubing.

The test rig's power supply consists of a 20 A, 24 VDC power supply with a 230 VAC single-phase input at CNR. The air compressor uses the same single-phase input, while the water pump requires a 380 VAC three-phase supply. All power is provided via the towing tank electrical powerplant.

Control of the test rig is handled via an HMI mounted to the control panel at the side of the test rig. Operators can vary the water and air flow rates by inputting the required values. The HMI also displays flow rates for all water lines, the total air flow, and a number of pressure measurements. Operators can also view the valve output percentage for troubleshooting purposes. The HMI can plot live data via a graphing screen. An SD card is fitted to the HMI, which logs data for further analysis.

Table 8: Bill of Material for Rig

P&ID Tag ID	Qty	Name	Maker	Mfgr Model/Part No	Connection Size	Connection Type	Material	Electrical	Scope of Supply
P-100	1	Water Pump	Conforto	STM6	Inlet: 1-1/4" Outlet: 1"	Threaded	Brass impeller, pump body G20 cast iron base support AISI 416 stainless steel shaft Ceramic/graphite mechanical seal	3-phase - CNR to connect	CNR
HV-101	1	Isolation Valve - Water Inlet	Georg Fischer	161375543	25 mm	Spigot	PVC-U	-	Armada
FIT-100	1	Flow Meter - Water Inlet	Endress & Hauser	DMA20-AAAAA1	G3/4	Threaded	Stainless steel, PEEK, FKM seal	4-20 mA analogue output, 24 Vdc supply, M12 connector	Armada
FCV-100	1	Flow Control Valve - Water Inlet	Burkert	Type 3285, Article No. 269253	G3/4	Threaded	Brass body	4-20 mA analogue input, 24 Vdc supply, DIN connector	Armada
PIT-100	1	Pressure Transmitter - Water Inlet	if	PA3524	G1/4	Threaded	Stainless steel, FKM seal	4-20 mA analogue output, loop powered, M12 connector	Armada
HV-200	1	Isolation Valve - Air Inlet	Festo	QH-1/2	G1/2	Threaded	Brass, aluminium	-	Armada
PRV-200	1	Pressure Regulating Valve - Air Inlet	Festo	MS6-LFR-1/2-D7-E-R-V-WR)	G1/2	Threaded	Cast aluminium housing, NBR Seals	-	Armada
FIT-200	1	Flow Meter - Air Inlet	ifm	SD5000	G1/4	Threaded	Aluminium, stainless steel, FKM seal	4-20 mA analogue output, 24 Vdc supply, M12 connector	Armada
FCV-200	1	Flow Control Valve - Air Inlet	Burkert	Type 2871, Article No. 254453	G1/8	Threaded	Brass solenoid valve, FKM seals	24 Vdc coil fitted with an ASCO 8908A001 proportional 4-20mA control head	Armada
HV-200.1…14	14	Tuning Valve - Air Injection Lines	RS PRO	144-2662	6 mm	Push-Fit	PBT Resin	-	Armada
CV-200.1…14	14	Check Valve - Air Injection Lines	RS PRO	916-0943	6 mm	Push-Fit	Anodised Aluminium	-	Armada
PIT-200	1	Pressure Transmitter - Air Inlet	ifm	PA3524	G1/4	Threaded	Stainless steel, FKM seal	4-20 mA analogue output, loop powered, M12 connector	Armada
PIT-300	1	Pressure Transmitter - NBG Outlet	ifm	PA3524	G1/4	Threaded	Stainless steel, FKM seal	4-20 mA analogue output, loop powered, M12 connector	Armada
FIT-300	1	Flow Meter - Bubble Outlet Overflow	Endress & Hauser	DMA20-AAAAA1	G3/4	Threaded	Stainless steel, PEEK, FKM seal	4-20 mA analogue output, 24 Vdc supply, M12 connector	Armada
FCV-300	1	Flow Control Valve - Bubble Outlet Overflow	Burkert	Type 3285, Article No. 269253	G3/4	Threaded	Brass body	4-20 mA analogue input, 24 Vdc supply, DIN connector	Armada
T-300	1	20 L Water Storage Tank	Direct Water Tanks	T20NA4V12OUT	4" cap	Threaded	PE	-	Armada
HV-300	1	Isolation Valve - NBG Outlet	Direct Water Tanks	Part of T-300	1/2" BSP 12 mm Hosetail	Threaded	Brass	-	Armada
HV-300.1…14	14	Isolation Valve - Injection Lines	Festo	QH-1/2	G1/2	Threaded	Brass, aluminium	-	Armada
FIT-300.1…14	14	Flow Meter - Injection Lines	Endress & Hauser	DMA15-AAAAA1	G1/2 Male	Threaded	Stainless steel, PEEK, FKM seal	4-20 mA analogue output, 24 Vdc supply, M12 connector	Armada
FCV-300.1…14	14	Flow Control Valve - Injection Lines	Burkert	Type 2875, Article No. 255529	G1/2	Threaded	Brass solenoid valve, FKM seals	24 Vdc coil fitted with an ASCO 8908A001 proportional 4-20mA control head	Armada
HV-301.1…14	14	Tuning Valve - Injection Lines	STAUFF	DV-08-B-G	G1/4	Threaded	Zinc-plated steel	-	Armada
E-300.1…14	14	Injector	-	-	Water: G1/4 Air: 4 mm Barb	Threaded/Barb	PVDF	-	Armada

7 Injector (Outlet) Manufacturing

FRIENDSHIP SYSTEMS provided the geometries of the injectors for the two ships and CNR-INM designed the relative CAM models ready for manufacturing.

The injectors for the JBC model are aligned with the characteristics of the hull, namely a high-draught vessel operating at low speed. Conversely, the A2B vessel operates at higher speeds and has a relatively minor draught in comparison to JBC. These different characteristics exert an influence on the injector attributes. In fact, the A2B injector must deliver a higher effective flow rate, at a higher exit velocity, and with a shallower angle.

From a construction point of view, after the initial evaluation of different solutions based on technical and practical considerations, the injectors have been outsourced and produced by the 3D printing technology after the CNR-INM design. To guarantee a high-quality level of manufacturing, the injectors have been printed using the Tough 2000 resin by Formlabs (specs can be found at https://formlabs.com/uk/store/materials/tough-2000-resin/) which presents a strength and stiffness comparable to more expensive and renewed materials such as ABS. Each injector, both for the A2B and the JBC model, is composed of two parts, a main frame and the outlet. In Figure 21 the CAD files, which originated from the optimization process, and the final design are reported. The main frame, glued and screwed to the hull, hosts the outlet, which is held in place by screws while the presence of a custom rubber O-ring assures the water sealing. In addition to these two main parts, flat covers that can be mounted in the place of each and every outlet have been manufactured. These additional parts will allow additional measurements of the model resistance with only some of the outlets working, and the rest of them closed. By covering all the outlets, the baseline resistance could be recovered for comparison with preliminary results.

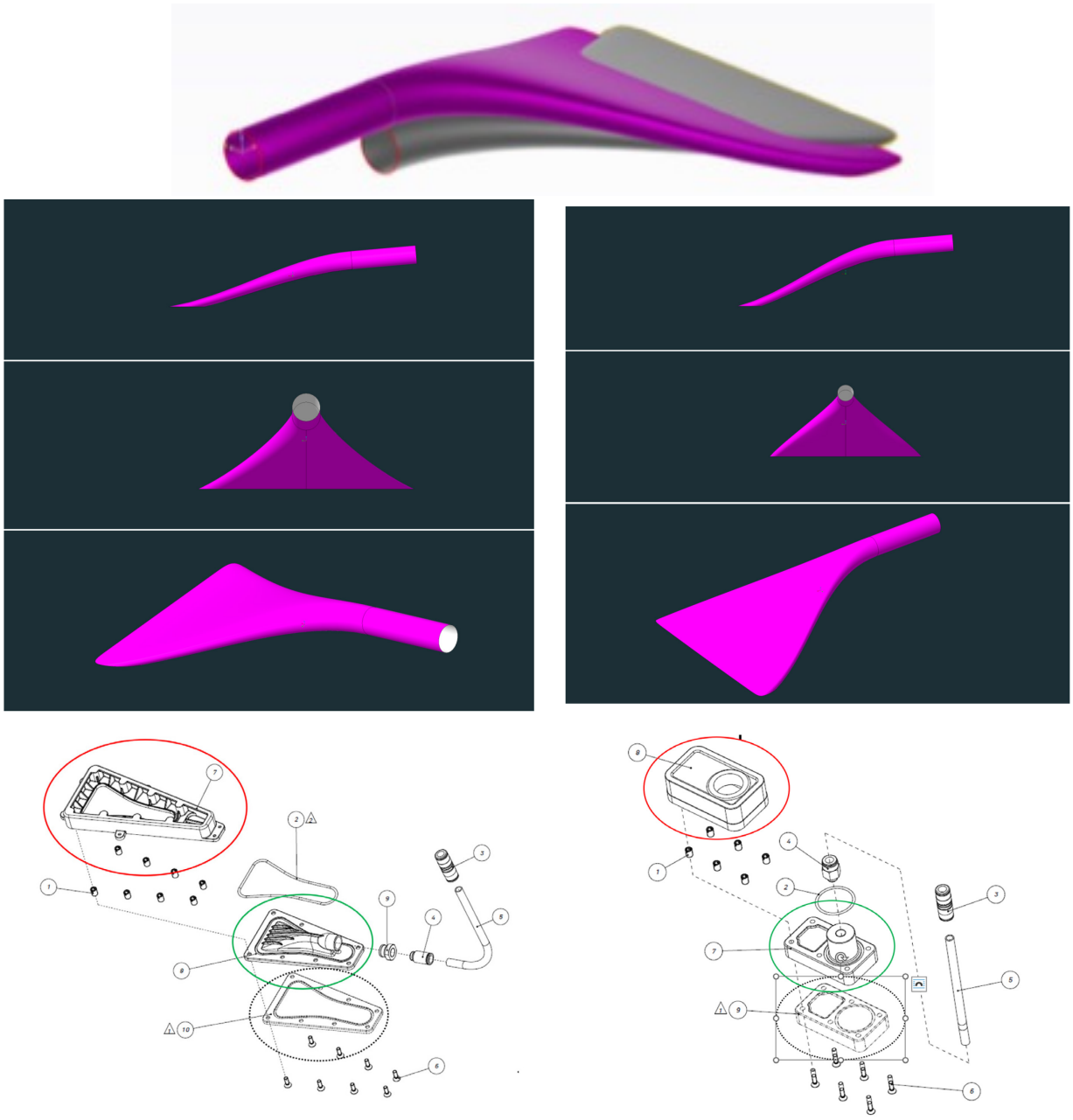

Figure 21: Engineering of the outlets. Concept (top rows, JBC in magenta, A2B in grey), outlets for A2B (middle row, left) and JBC (middle row, right) model, and design (bottom row). Frames (circled in red), outlets (circled in green) and covers (dash line)

To facilitate the assembly of the injectors, different apertures have been designed on the ship hulls, grouping some injectors in the same polyurethanic resin (or UREOL®, in light grey) in pocket due to the reduced mounting distance. The A2B model has been already finalised for the next tests with the PALS, see Figure 22, the JBC model is currently in preparation.

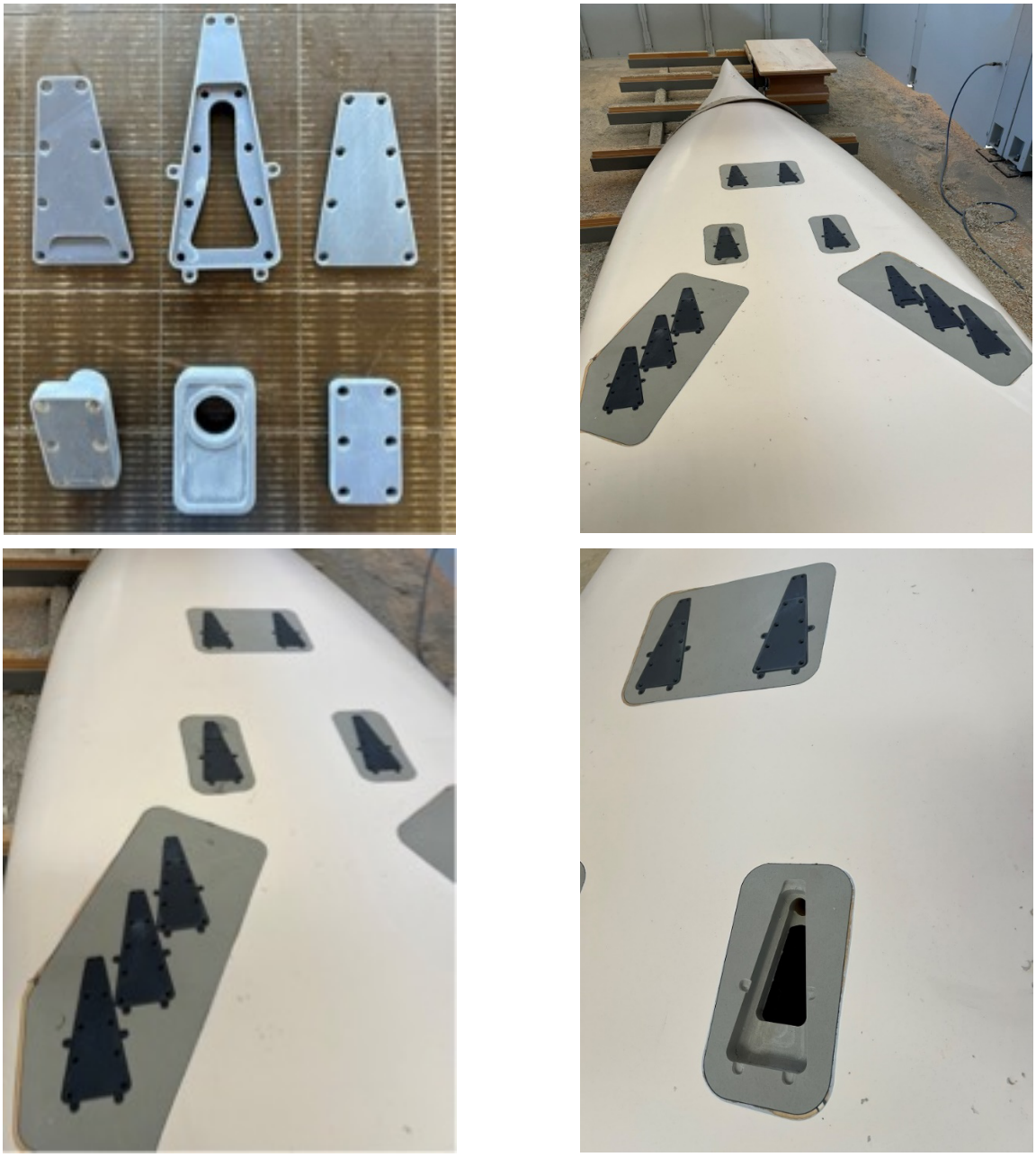

Figure 22: Outlets (top left, for A2B model above, for JBC below) and their installation in the A2B hull after machining.

8 Baseline Resistance Tests

8.1 Testing Methodology

The techniques adopted by CNR-INM for testing a conventional displacement vessel and analysing the test data are those suggested in [43] to assure repeatability and comparability among different Towing Tanks.

The model is run in the bare hull and appended conditions over the speed range, covering all the speeds of interest for the corresponding ship to construct the so-called resistance curve. Turbulence stimulators are fitted to the bare hull, whereas all the model appendages and rudders are not installed in this specific configuration.

The model is connected to the carriage via two fore and aft gimbals that measure draft variations during runs. When advancing, the model is free to roll, surge, heave, and trim. The surge is limited due to the force transducer and the tow rope connecting the model to the carriage. The roll, due to the symmetry, is nearly equal to zero. The model is aligned with the tracks along the tank.

The test sequence uses a variable number of runlets per carriage run, depending on the speeds. Generally, the mean waiting time between the runs is about 20/30 minutes. Zeroes of all quantities are recorded before each test day and used to net off the acquired data.

At CNR-INM, the ITTC'57 Method [43] is generally adopted; this method is based on Froude's principle and the "ITTC'57 model-ship correlation line". The resistance versus speed values obtained from the towing tests are reduced to a non-dimensional form. The total resistance coefficient is defined as:

$$C_{TM} = \frac{R_{TM}}{\frac{1}{2}\rho_M S_M V_M^2} \tag{9}$$

where the subscript *T* stands for total, and *M* refers to the model scale.

The "skin friction" component of resistance of the model is estimated for each experiment speed using the ITTC'57 correlation line:

$$C_F = \frac{0.075}{(\log_{10} Re - 2)^2} \tag{10}$$

where the subscript *F* stands for frictional and the Reynolds number, Re, is evaluated on the overall submerged length of the model, the model speed (imposed by the carriage), and the tank water viscosity

$$Re = \frac{VL}{\upsilon} \tag{11}$$

The frictional resistance coefficient is subtracted from the total resistance coefficient to obtain the residual resistance coefficient C_R:

$$C_R = C_{TM} - C_{FM} \tag{12}$$

The total resistance coefficient C_{TM} and the frictional one C_{FM} are plotted against model Reynolds number Re appropriate to the model length and tank water viscosity, and a mean line is drawn through the experiment points. The residual resistance coefficient values are plotted against the Fr number:

$$Fr = \frac{V}{\sqrt{gL}} \tag{13}$$

Due to the application of interest in the context of RETROFIT55, which makes the correlation model inapplicable due to the simultaneous presence of different physical phenomena, the extrapolation of the results to the full scale is not presented. On this basis, the total resistance of the model versus the advancing speed and the standard coefficients will be presented in Section 8.3. The main aim is to evaluate the three components of the resistance to lay down a basis for evaluating the lubrication effectiveness.

8.2 Instrumentation

8.2.1 Load Cells

Force transducers (or load cells) are utilized to directly measure the hull's resistance in the towing test's classical set-up. During the acceleration/deceleration part of the carriage run, the model is clamped to the carriage, and no measurement is performed. When constant speed is reached (the selected test speed), the clamp is opened, and the hull is connected to the carriage through the load cell, measuring the resistance force. Depending on the kind of the ship under testing, a second, additional load cell is used. This cell is pre-loaded with a known weight to increase the hull's resistance and its dynamic stability.

The force transducers used in the current test campaign are from HBM, model U1. The measuring element is a high-grade hardened and tempered steel spring on which four strain gauges are mounted so that two of them are extended and the other two are compressed when the measuring spring is loaded in the measuring direction. Transducers incorporate a housing that hermetically seals the measuring element. This housing is mechanically connected to the measuring element via bellows (or diaphragms). This configuration prevents significant components of the measured load from being transferred to the housing, thereby ensuring accurate measurement results.

According to the INM procedure, the transducers are calibrated before the tests. The calibration is performed according to the European Standards guidelines. The transduces are calibrated with high-quality reference weights using Remmers support equipment, performing repeatability and a hysteresis loop. The same load cells have been used for the two investigated hull models, and calibrations have been repeated before each of the two campaigns.

The expanded uncertainty, which is the value to consider as a general indication, is very reduced, being well below 1%. Assuming this value, which can be taken as an estimate of the error in the resistance measurement, it is possible to deduce that when the air lubrication system will be working, frictional resistance reduction higher than 1.5% of the original value will be effectively measured, estimating this contribute to be about 70% of the total resistance.

8.2.2 Immersion Gauges

To measure the hull's immersion, two in-house, developed devices (or immersion gauges) have been used at fore and aft longitudinal positions, respectively (positions may differ for each tested model).

The present device converts a vertical displacement into an angular one through a mechanical parallelogram (or pantograph). In particular, the device is composed of two arms and two cylindrical joints, see Figure 23. Adding a set of adequate weights, with adjustable position, to the device does not perturb or constrain the vertical motion of the hull (to which the device is attached), which is free to move and oscillate. During the acquisition of the resistance, the model is connected to the carriage using these two devices, which are rigidly connected to the carriage rails.

Two gimbals connect the devices to the hull, allowing roll and pitch motions. In this way, the model is free to modify its trim and sinkage by modifying its fore and aft immersion. Encoders are mounted on the rotation axes of the arms (two encoders per immersion gauge) to measure the rotations recorded by the acquisition system and convert them into vertical translation.

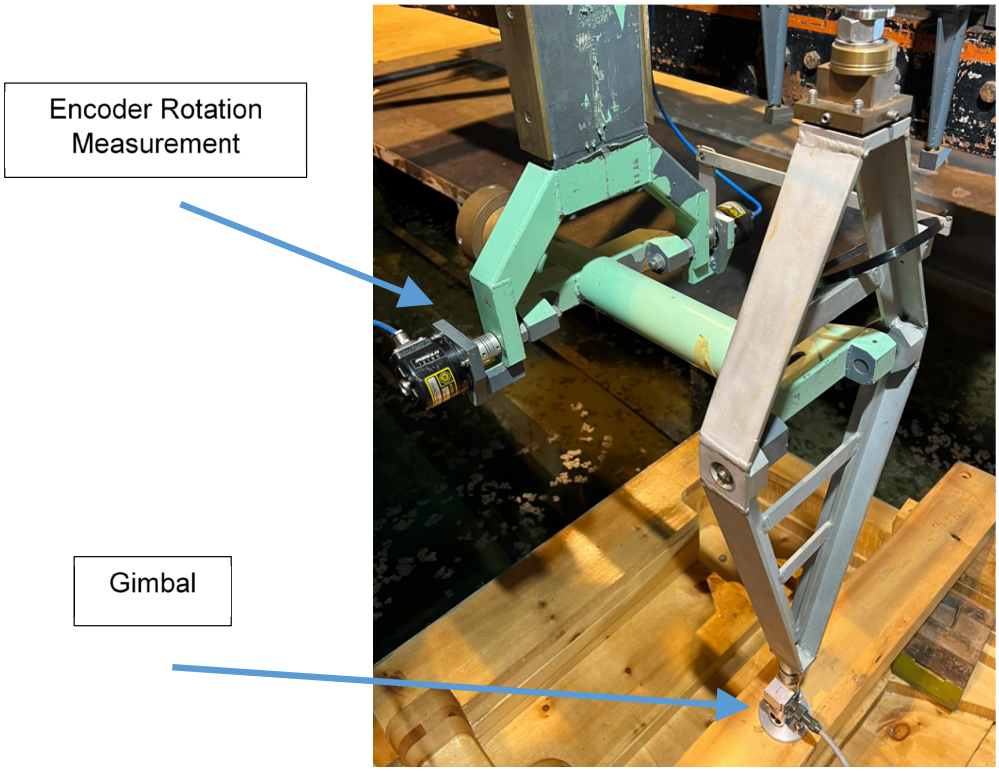

Figure 23: Immersion gauge.

In Figure 24 the mechanical scheme of the immersion gauge is reported at rest (or in steady condition for hull taken as zero or reference position) and when displaced. Based on the mechanical scheme adopted, the following formula permits to derive the vertical translation from the rotations of the two joints:

$$\Delta = L1 \cdot \sin\alpha + L2 \cdot (1 - \cos\beta) \tag{14}$$

L1 and L2 are equal to 300 and 500 mm in the used device, respectively. The encoders employed are incremental with a Z signal. The resolution is 3600 pulses (steps)/round, which gives an angular resolution of 0.1°. On this basis, the vertical resolution in position (assuming a rotation of 1 step per encoder) is equal to 0.524mm.

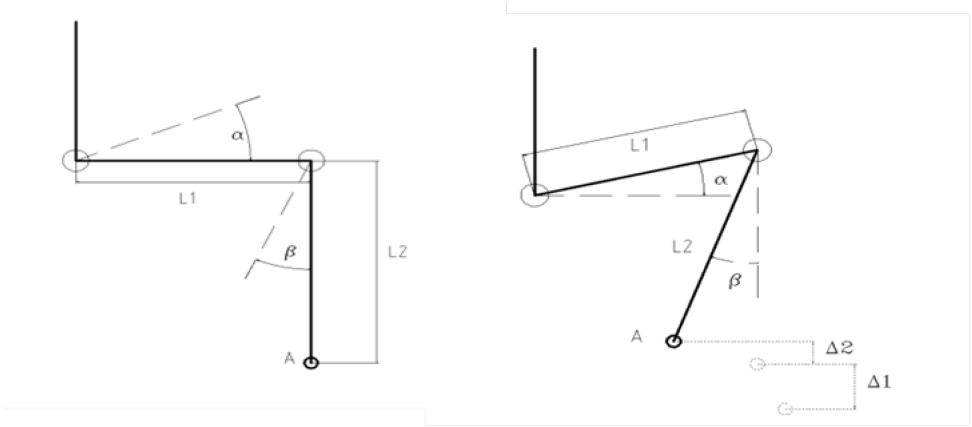

Figure 24: Mechanical Sketch in zero position (left) and measuring (right)

8.2.3 Acquisition System

The signals from the transducers (force and immersion) are transmitted to the data acquisition system by flexible, dedicated cables. The Dewesoft DEWE-43™ system consists of 8 anti-aliased, dynamic simultaneous sampled 24-bit analog inputs, with a front-end amplifier for voltage and strain sensors (200 kHz/channel maximum sampling rate and 32 for oversampled sigma-delta A/D per channel). Furthermore, 8 Counters/digital inputs are capable of 1 for event count, encoder, period, and frequency measurement per channel. These counter inputs are fully synchronized with analog data. The hardware provides necessary electrical excitation to measurement transducers, converts electric signals generated for the data acquisition board, amplifies the signal level to the A/D converter level, and makes analog-to-digital (A/D) conversion. The DEWE-43 is connected to the computer via a USB interface. A DEWESoft application software analyses the signals and exports them to almost any analysis package.

8.3 Results

8.3.1 A2B Model

This ship model has been tested in full loading and trial loading conditions. The hull has been tested in fully appended and bare hull configuration in both conditions. Because of the kind of ship, the fully appended configuration is characterized by the presence of a gate rudder only. For each loading condition and geometrical configuration, the total resistance has been measured for seven advancing speeds, ranging from 10 to 16 knots (at full scale) in step of 1kn.

The correspondence between the ship velocity (in knots) and the scale model (m/s) is given in the following Table 9.

Table 9: Velocities, Froude, and Reynolds number (model scale).

V ship (kn)	V model (m/s)	F_n	Rn_m (*10^{-6})
10	1.165	0.148	7.389
11	1.281	0.163	8.125

12	1.398	0.178	8.867
13	1.514	0.192	9.603
14	1.631	0.207	10.345
15	1.747	0.222	11.081
16	1.864	0.237	11.823

According to CNR-INM nomenclature, four different configurations have been named, each with a loading condition and a hull configuration:

- Series 1 - Full loading condition, with appendages (also FL with appendages)
- Series 2 - Trial loading condition, with appendages (also TL with appendages)
- Series 3 – Full loading condition, bare hull (also FL, bare hull)
- Series 4 – Trial loading condition, bare hull (TL, bare hull).

Data are reported in tabular format for each series by the standard used at CNR-INM, as seen in Figure 25, and then graphics are provided in Figure 26. Data are shown both in dimensional and non-dimensional form for each measuring condition, and finally, some comparisons are made. Slight differences are observed between the bare hull and the fully appended configurations, as expected due to the reduced area of the gate rudders. On the contrary, larger differences in all the resistance coefficients are found between the full loading and the trail loading conditions, reflecting the excellent performance of the hull in full loaded conditions that degrades when working out of the design displacement. Also, due to the short velocity range investigated, all the resistance coefficients display a weak dependence on the velocity; at the highest velocities, as usual for this kind of ship, the residual resistance coefficient starts to increase with a simultaneous decrease of the frictional resistance coefficient. In any case, the frictional resistance is always well above 70% of the total resistance and above 80% in most of the range.

Ship Model No:2639- Test No:001

Resistance test results

Scale ratio	λ	19.50		
Temperature of sea water (std)	t_s	15.00		°C
Temperature of tank water	t_m	20.30		°C
Viscosity of sea water (std)	ν_s	1.1892	$*10^{-6}$	m^2/s
Viscosity of tank water	ν_m	0.9961	$*10^{-6}$	m^2/s
Mass density of sea water	ρ_s	1026.021		Kg/m^3
Mass density of tank water	ρ_m	998.145		Kg/m^3
Incremental resistance coefficient	Δc	2.000	$*10^{-4}$	
Form Factor	$1+k$	1.000		

Length between perpendiculars	L_{PP}	120.400	m
Length of waterline	L_{WL}	123.201	m
Length overall submerged	L_{OS}	123.201	m
Breadth moulded max	B_M	21.750	m
Breadth of waterline	B_{WL}	21.750	m
Draft at forward perpendicular	T_F	5.500	m
Draft at afterward perpendicular	T_A	5.500	m
Draft at midship	T_M	5.500	m
Displacement weight	Δ	9340	t
Area of wetted surface	S_S	2944.05	m^2
Block coefficient	C_B	0.6183	

V_m m/s	RT_m N	CT_m $*10^3$	CF_m $*10^3$	RN_m $*10^{-6}$	CR $*10^3$	CT_s $*10^3$	V_s Knots	RT_s kN	PEF kW	PE kW	F_n	$F_{n\nabla}$	CT_∇	DTF m	DTA m
1.165	19.646	3.746	3.164	7.389	0.582	2.439	10.00	97.5	382.0	501.7	0.148	0.360	16.473	0.129	0.010
1.281	23.204	3.659	3.111	8.125	0.548	2.386	11.00	115.3	502.3	652.2	0.163	0.395	16.110	0.154	0.018
1.398	27.204	3.602	3.064	8.867	0.539	2.358	12.00	135.7	646.4	837.8	0.178	0.431	15.922	0.193	0.025
1.514	31.753	3.585	3.021	9.603	0.564	2.366	13.00	159.8	813.7	1068.1	0.192	0.467	15.981	0.236	0.033
1.631	36.449	3.546	2.982	10.345	0.563	2.351	14.00	184.2	1008.8	1326.8	0.207	0.503	15.878	0.276	0.043
1.747	42.644	3.616	2.947	11.081	0.669	2.443	15.00	219.6	1230.2	1693.9	0.222	0.539	16.496	0.316	0.053
1.864	50.526	3.763	2.915	11.823	0.849	2.610	16.00	267.1	1483.6	2198.5	0.237	0.575	17.626	0.362	0.064

11/12/2023 12:57

Ship Model No:2639- Test No:002

Resistance test results

Scale ratio	λ	19.50		
Temperature of sea water (std)	t_s	15.00		°C
Temperature of tank water	t_m	20.00		°C
Viscosity of sea water (std)	ν_s	1.1892	$*10^{-6}$	m^2/s
Viscosity of tank water	ν_m	1.0034	$*10^{-6}$	m^2/s
Mass density of sea water	ρ_s	1026.021		Kg/m^3
Mass density of tank water	ρ_m	998.207		Kg/m^3
Incremental resistance coefficient	Δc	2.000	$*10^{-4}$	
Form Factor	$1+k$	1.000		

Length between perpendiculars	L_{PP}	120.400	m
Length of waterline	L_{WL}	116.522	m
Length overall submerged	L_{OS}	118.610	m
Breadth moulded max	B_M	21.750	m
Breadth of waterline	B_{WL}	21.750	m
Draft at forward perpendicular	T_F	2.800	m
Draft at afterward perpendicular	T_A	4.150	m
Draft at midship	T_M	3.475	m
Displacement weight	Δ	5387	t
Area of wetted surface	S_S	2275.27	m^2
Block coefficient	C_B	0.5863	

V_m m/s	RT_m N	CT_m $*10^3$	CF_m $*10^3$	RN_m $*10^{-6}$	CR $*10^3$	CT_s $*10^3$	V_s Knots	RT_s kN	PEF kW	PE kW	F_n	$F_{n\nabla}$	CT_∇	DTF m	DTA m
1.165	15.764	3.890	3.190	7.062	0.700	2.566	10.00	79.3	296.5	407.8	0.151	0.394	19.328	0.044	0.087
1.281	18.871	3.847	3.136	7.768	0.711	2.556	11.00	95.6	390.3	540.7	0.166	0.434	19.254	0.045	0.107
1.398	22.381	3.834	3.088	8.474	0.746	2.573	12.00	114.5	501.7	706.6	0.181	0.473	19.380	0.049	0.133
1.514	26.038	3.801	3.045	9.181	0.756	2.566	13.00	134.0	632.2	896.0	0.196	0.512	19.330	0.057	0.161
1.631	30.263	3.809	3.006	9.887	0.803	2.598	14.00	157.3	783.0	1133.2	0.211	0.552	19.572	0.071	0.190
1.747	34.664	3.801	2.970	10.593	0.831	2.612	15.00	181.6	955.6	1401.2	0.226	0.591	19.677	0.085	0.215
1.864	39.488	3.806	2.937	11.299	0.869	2.637	16.00	208.6	1151.4	1716.8	0.241	0.631	19.865	0.095	0.235

11/12/2023 12:59

Ship Model No:2639- Test No:003

Resistance test results

Scale ratio	λ	19.50		
Temperature of sea water (std)	t_s	15.00		°C
Temperature of tank water	t_m	19.00		°C
Viscosity of sea water (std)	ν_s	1.1892	$*10^{-6}$	m^2/s
Viscosity of tank water	ν_m	1.0283	$*10^{-6}$	m^2/s
Mass density of sea water	ρ_s	1026.021		Kg/m^3
Mass density of tank water	ρ_m	998.408		Kg/m^3
Incremental resistance coefficient	Δc	2.000	$*10^{-4}$	
Form Factor	$1+k$	1.000		

Length between perpendiculars	L_{pp}	120.400	m
Length of waterline	L_{WL}	123.201	m
Length overall submerged	L_{OS}	123.201	m
Breadth moulded max	B_M	21.750	m
Breadth of waterline	B_{WL}	21.750	m
Draft at forward perpendicular	T_F	5.500	m
Draft at afterward perpendicular	T_A	5.500	m
Draft at midship	T_M	5.500	m
Displacement weight	Δ	9340	t
Area of wetted surface	S_S	2903.02	m^2
Block coefficient	C_B	0.6183	

V_m m/s	RT_m N	CT_m $*10^3$	CF_m $*10^3$	RN_m $*10^{-6}$	CR $*10^3$	CT_s $*10^3$	V_s Knots	RT_s kN	PEF kW	PE kW	F_n	$F_{n\nabla}$	CT_∇	DTF m	DTA m
1.165	18.901	3.655	3.182	7.158	0.472	2.330	10.00	91.8	376.7	472.5	0.148	0.360	15.515	0.135	0.008
1.281	22.597	3.610	3.129	7.874	0.482	2.319	11.00	110.6	495.9	625.8	0.163	0.396	15.441	0.169	0.018
1.398	26.557	3.566	3.081	8.589	0.485	2.304	12.00	130.8	637.4	807.3	0.178	0.431	15.342	0.201	0.024
1.514	30.939	3.539	3.038	9.305	0.501	2.304	13.00	153.5	803.1	1026.3	0.192	0.467	15.340	0.236	0.029
1.631	35.870	3.538	2.999	10.021	0.539	2.327	14.00	179.8	994.7	1294.8	0.207	0.503	15.497	0.277	0.035
1.747	41.968	3.606	2.963	10.737	0.643	2.417	15.00	214.3	1214.0	1653.9	0.222	0.539	16.093	0.322	0.044
1.864	49.585	3.745	2.931	11.453	0.814	2.576	16.00	259.9	1462.8	2139.1	0.237	0.575	17.150	0.367	0.061

Ship Model No:2639- Test No:004

Resistance test results

Scale ratio	λ	19.50		
Temperature of sea water (std)	t_s	15.00		°C
Temperature of tank water	t_m	19.00		°C
Viscosity of sea water (std)	ν_s	1.1892	$*10^{-6}$	m^2/s
Viscosity of tank water	ν_m	1.0283	$*10^{-6}$	m^2/s
Mass density of sea water	ρ_s	1026.021		Kg/m^3
Mass density of tank water	ρ_m	998.408		Kg/m^3
Incremental resistance coefficient	Δc	2.000	$*10^{-4}$	
Form Factor	$1+k$	1.000		

Length between perpendiculars	L_{pp}	120.400	m
Length of waterline	L_{WL}	116.522	m
Length overall submerged	L_{OS}	118.610	m
Breadth moulded max	B_M	21.750	m
Breadth of waterline	B_{WL}	21.750	m
Draft at forward perpendicular	T_F	2.800	m
Draft at afterward perpendicular	T_A	4.150	m
Draft at midship	T_M	3.475	m
Displacement weight	Δ	5387	t
Area of wetted surface	S_S	2234.24	m^2
Block coefficient	C_B	0.5863	

V_m m/s	RT_m N	CT_m $*10^3$	CF_m $*10^3$	RN_m $*10^{-6}$	CR $*10^3$	CT_s $*10^3$	V_s Knots	RT_s kN	PEF kW	PE kW	F_n	$F_{n\nabla}$	CT_∇	DTF m	DTA m
1.165	15.283	3.838	3.204	6.891	0.634	2.500	10.00	75.8	291.2	390.1	0.151	0.394	18.488	0.027	0.087
1.281	18.401	3.820	3.150	7.580	0.671	2.516	11.00	92.3	383.3	522.6	0.166	0.434	18.608	0.035	0.113
1.398	21.783	3.800	3.102	8.269	0.699	2.526	12.00	110.3	492.7	681.1	0.181	0.473	18.680	0.042	0.138
1.514	25.479	3.787	3.058	8.958	0.729	2.540	13.00	130.2	620.7	870.8	0.196	0.512	18.785	0.049	0.163
1.631	29.498	3.781	3.019	9.648	0.762	2.557	14.00	152.0	768.8	1095.2	0.211	0.552	18.915	0.058	0.188
1.747	33.831	3.777	2.983	10.337	0.794	2.575	15.00	175.8	938.3	1356.4	0.226	0.591	19.048	0.072	0.214
1.864	38.664	3.794	2.950	11.026	0.844	2.613	16.00	202.9	1130.6	1670.1	0.241	0.631	19.325	0.093	0.241

Figure 25: Test data of the four series of the A2B model

Figure 26 shows the resistance components at different ship velocity.

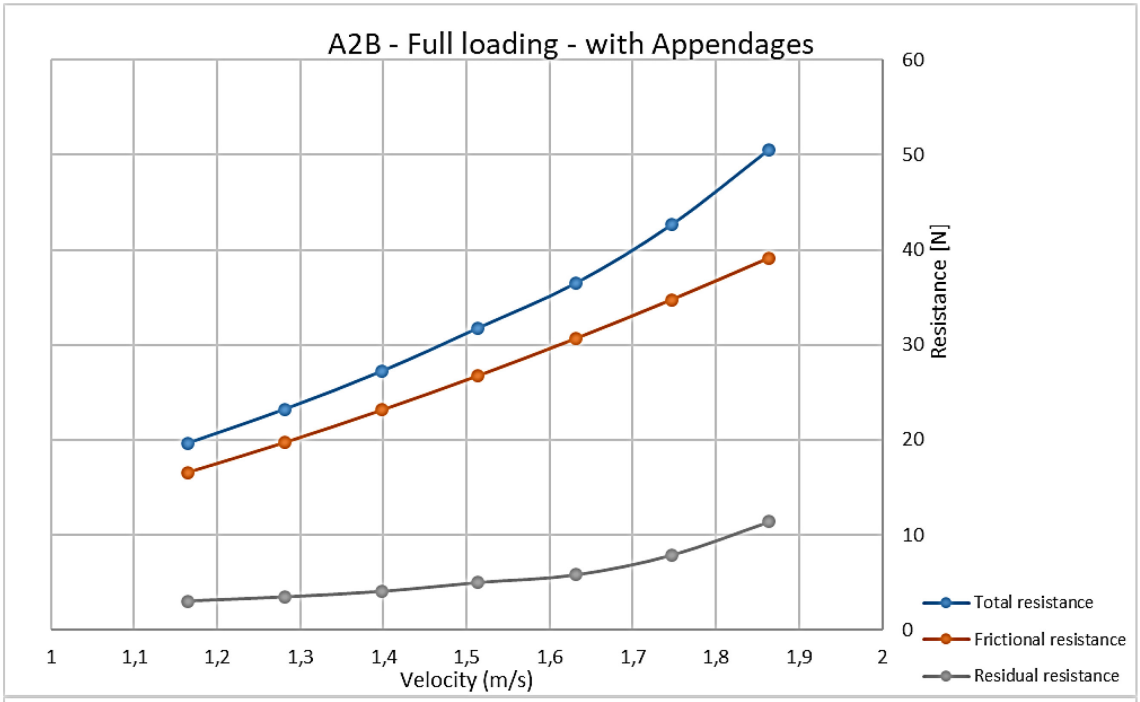

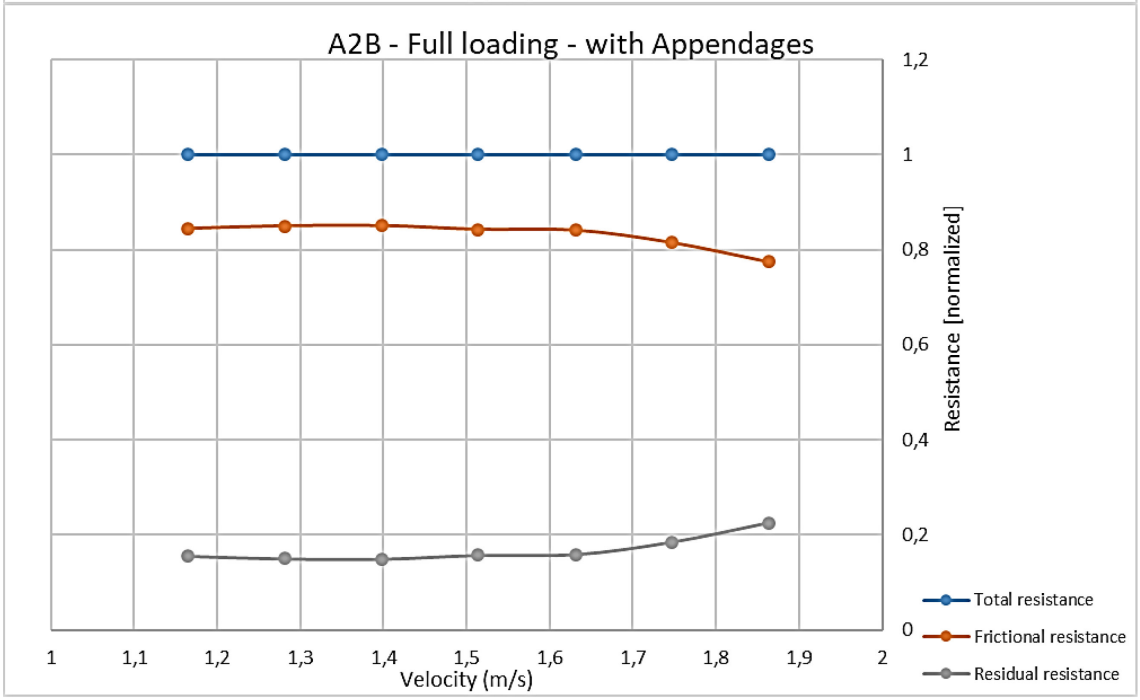

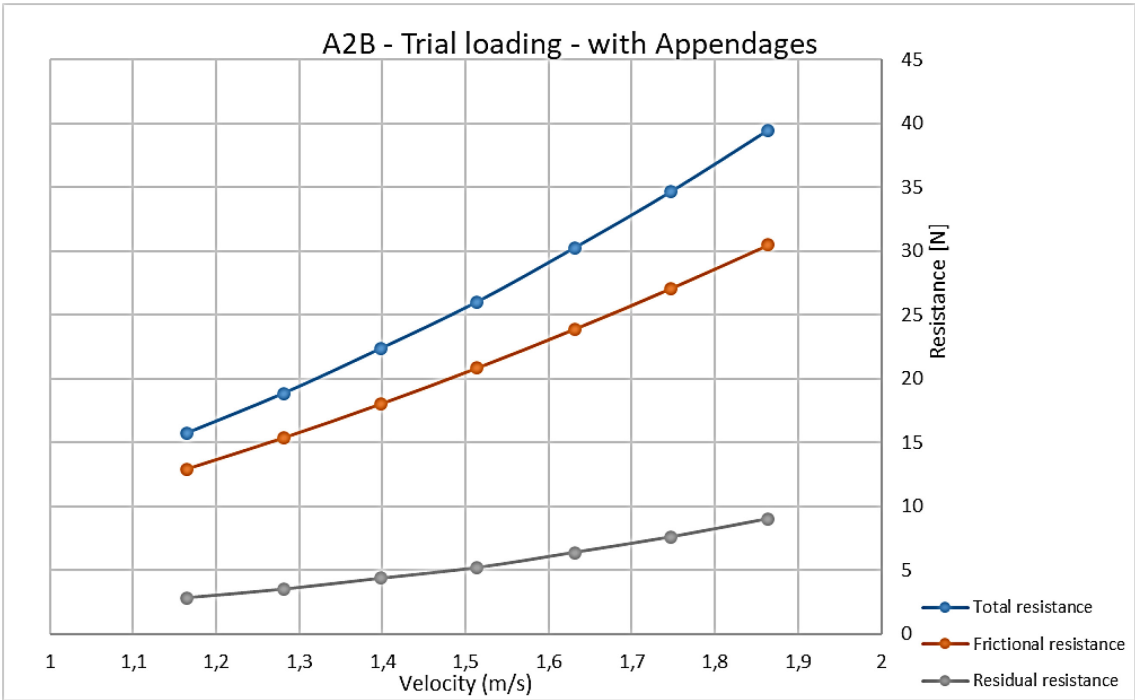
A2B - Trial loading - with Appendages
45
40
35
30
25
20
15
10
5
0
Resistance [N]
1
1,1
1,2
1,3
1,4
1,5
1,6
1,7
1,8
1,9
2
Velocity (m/s)
Total resistance
Frictional resistance
Residual resistance

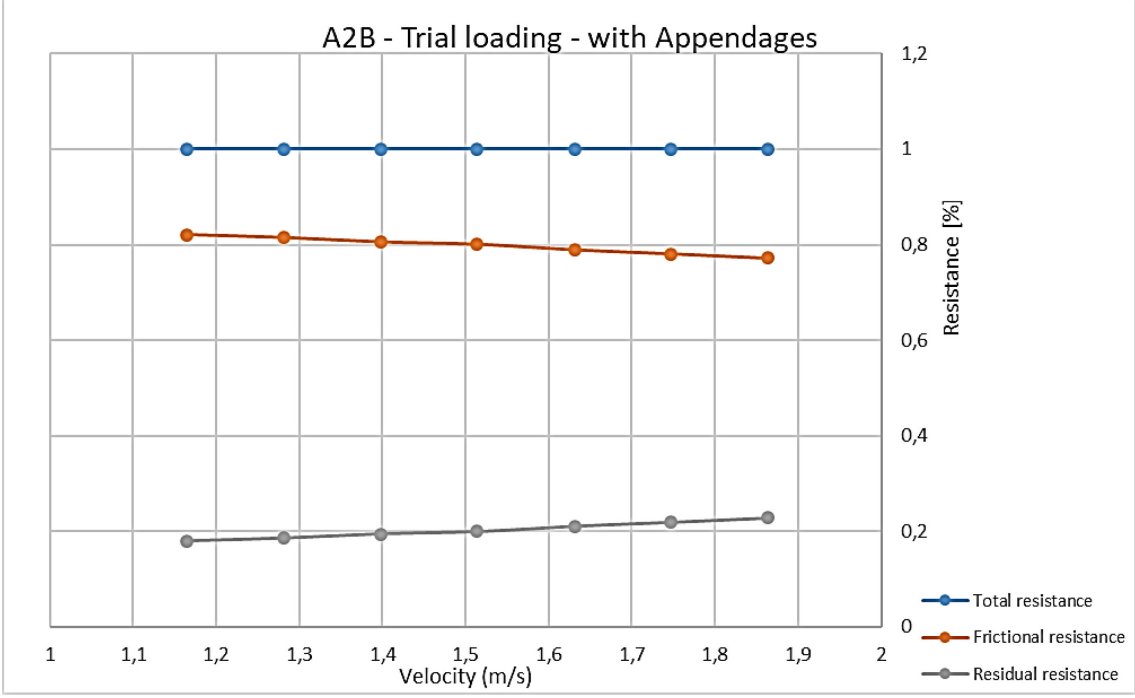
A2B - Trial loading - with Appendages
1,2
1
0,8
0,6
0,4
0,2
0
Resistance [%]
1
1,1
1,2
1,3
1,4
1,5
1,6
1,7
1,8
1,9
2
Velocity (m/s)
Total resistance
Frictional resistance
Residual resistance

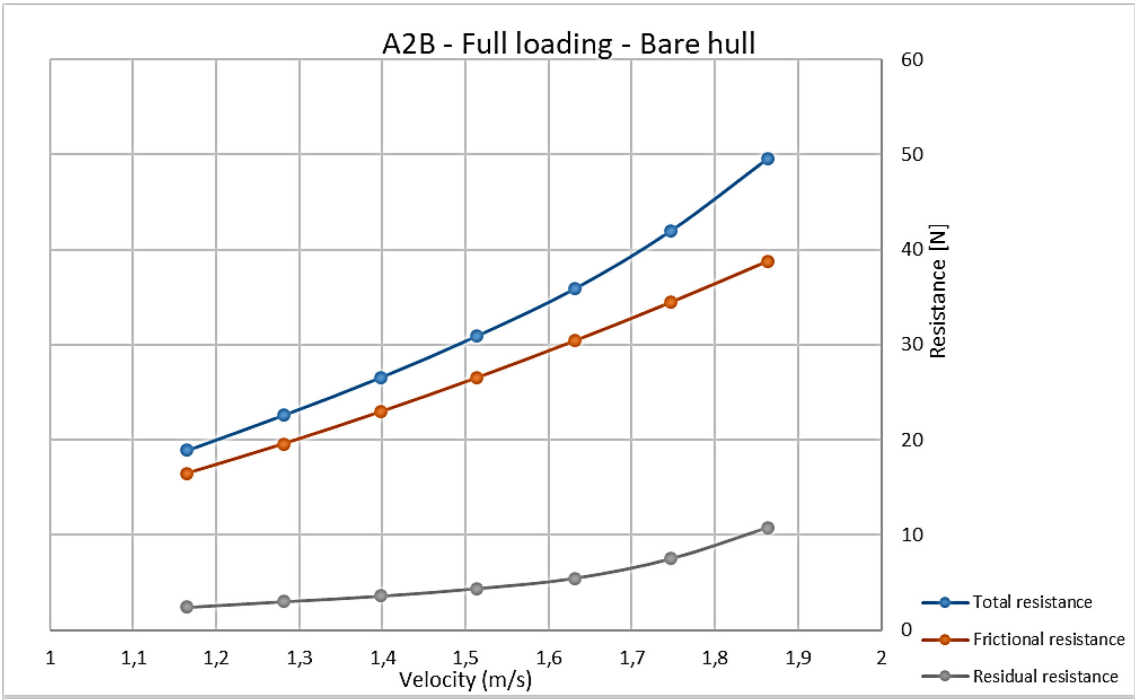
A2B - Full loading - Bare hull
60
50
40
30
20
10
0
Resistance [N]
1
1,1
1,2
1,3
1,4
1,5
1,6
1,7
1,8
1,9
2
Velocity (m/s)
Total resistance
Frictional resistance
Residual resistance

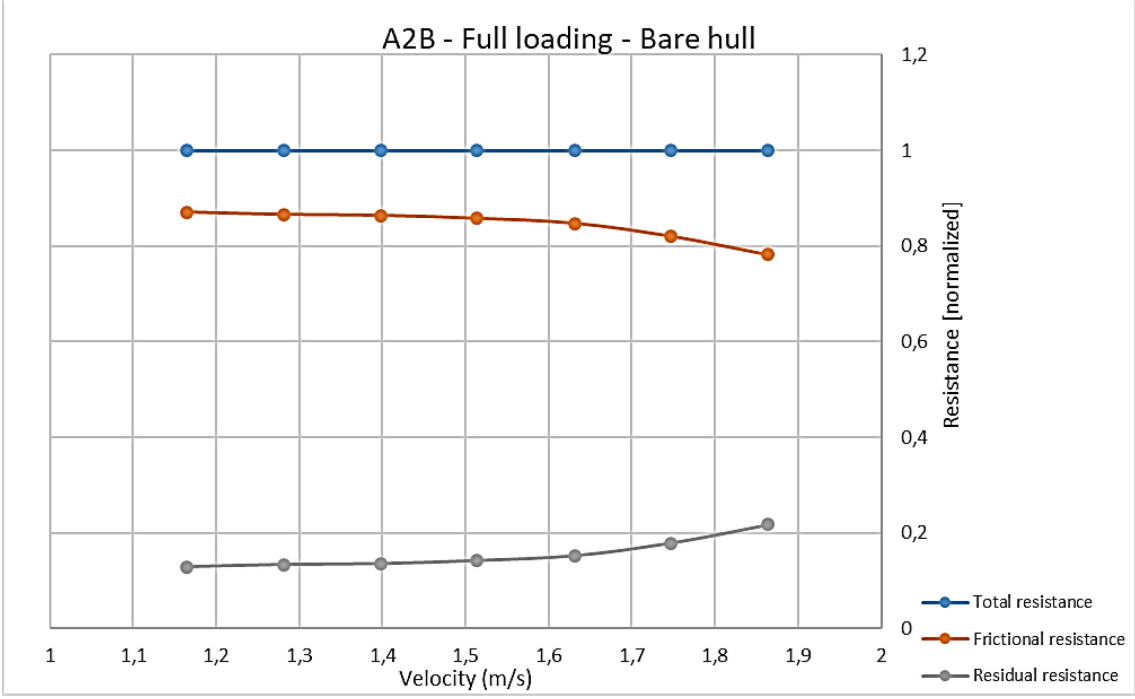
A2B - Full loading - Bare hull
1,2
1
0,8
0,6
0,4
0,2
0
Resistance [normalized]
1
1,1
1,2
1,3
1,4
1,5
1,6
1,7
1,8
1,9
2
Velocity (m/s)
Total resistance
Frictional resistance
Residual resistance

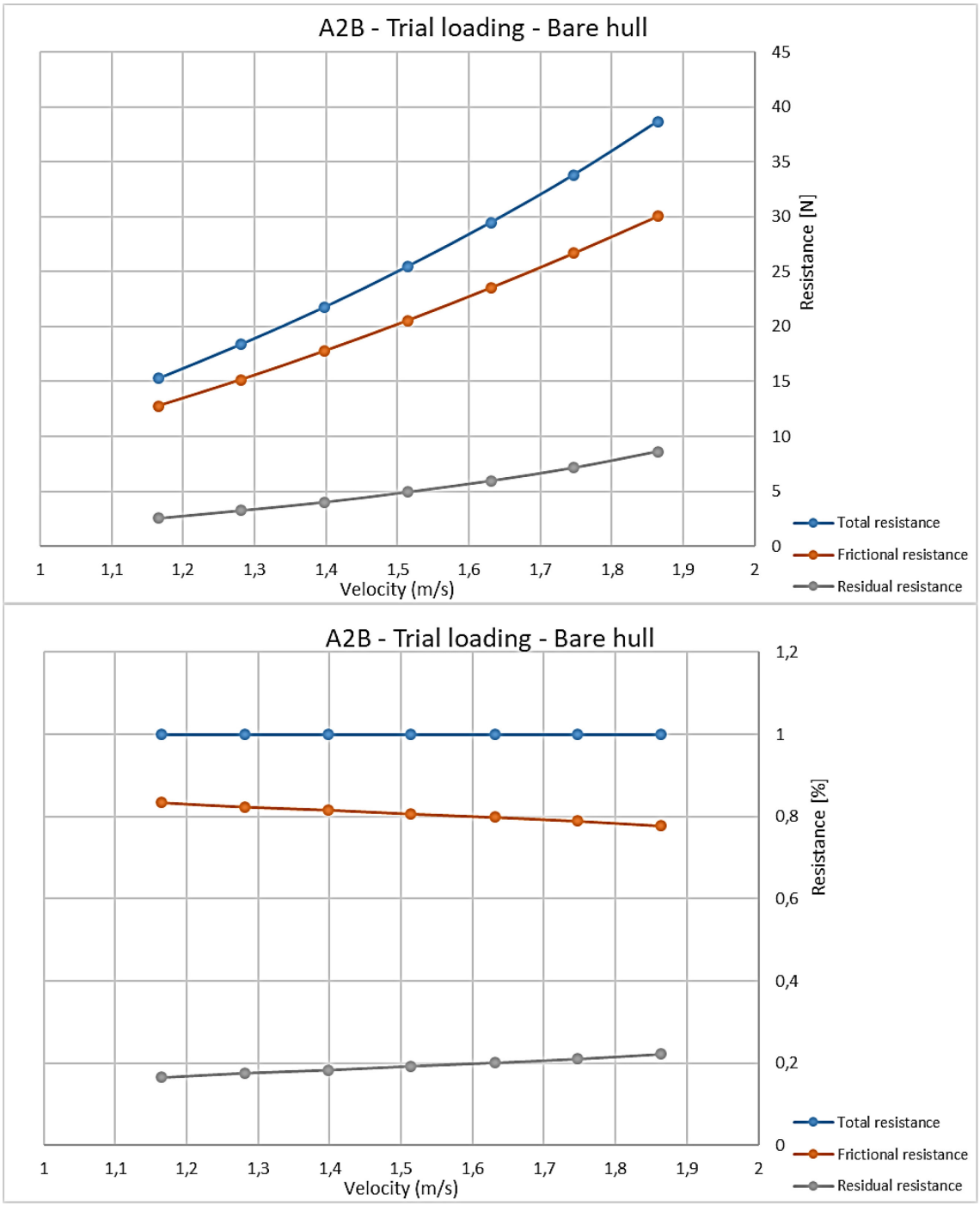

Figure 26: A2B graphical results

8.3.2 JBC Model

This ship model has been tested in full loading and trial loading conditions. In both conditions, the hull has been tested in bare hull configuration only. For each loading condition, the total resistance has been measured in a large interval of advancing speed, ranging from 4 to 22 knots (at full scale) in step of 1 kn. The correspondence between the ship velocity at full scale (in knots) and the scale model (in m/s) is given in the following Table 10, together with Froude and Reynolds number.

Table 10: Velocities, Froude and Reynolds number (model scale).

V ship [kn]	V model [m/s]	Fr	Re_m (*10^{-6})
4	0.275	0.039	1.494
5	0.344	0.048	1.869
6	0.412	0.058	2.238
7	0.481	0.067	2.613
8	0.550	0.077	2.988
9	0.619	0.087	3.363
10	0.688	0.096	3.732
11	0.756	0.106	4.107
12	0.825	0.116	4.482
13	0.894	0.125	4.856
14	0.962	0.135	5.226
14.5	0.997	0.140	5.416
15	1.031	0.145	5.601
15.5	1.066	0.149	5.791
16	1.100	0.154	5.976
17	1.169	0.164	6.350
18	1.237	0.173	6.720
19	1.306	0.183	7.095
20	1.375	0.193	7.469
21	1.444	0.202	7.844
22	1.512	0.212	8.214

According to CNR-INM nomenclature, four different configurations have been named, each with a loading condition and a hull configuration:

- Series 1 – Full loading condition, bare hull (also FL, bare hull)
- Series 2 – Trail loading condition, bare hull (also TL, bare hull).

Data are reported in tabular format for each series, see Figure 27, and in graphical form (Figure 28). In addition, data are shown both in dimensional and non-dimensional form for each condition. For this model, a larger velocity interval has been investigated. The low range of the velocity interval is generally dedicated to the evaluation of the *k* coefficient or form factor which accounts for any 3D effect, whereas the high velocity range is investigated to find out the velocity above which the wave resistance component starts to increase rapidly, indicating the end of the operative range for the selected ship.

Ship Model No:2641- Test No:001

Resistance test results

Scale ratio	λ	56.00	
Temperature of sea water (std)	t_s	15.00	°C
Temperature of tank water	t_m	22.00	°C
Viscosity of sea water (std)	ν_s	1.1892	$*10^{-6}$ m²/s
Viscosity of tank water	ν_m	0.9565	$*10^{-6}$ m²/s
Mass density of sea water	ρ_s	1026.021	Kg/m³
Mass density of tank water	ρ_m	997.774	Kg/m³
Incremental resistance coefficient	Δc	2.000	$*10^{-4}$
Form Factor	$1+k$	1.000	

Length between perpendiculars	L_{pp}	280.000	m
Length of waterline	L_{WL}	285.000	m
Length overall submerged	L_{OS}	290.976	m
Breadth moulded max	B_M	45.000	m
Breadth of waterline	B_{WL}	45.000	m
Draft at forward perpendicular	T_F	16.500	m
Draft at afterward perpendicular	T_A	16.500	m
Draft at midship	T_M	16.500	m
Displacement weight	Δ	178369	t
Area of wetted surface	S_S	19556.10	m²
Block coefficient	C_B	0.8055	

V_m m/s	RT_m N	CT_m $*10^3$	CF_m $*10^3$	RN_m $*10^{-6}$	CR $*10^3$	CT_s $*10^3$	V_s Knots	RT_s kN	PEF kW	PE kW	F_n	$F_{n\nabla}$	CT_∇	DTF m	DTA m
0.275	1.196	5.083	4.304	1.494	0.779	2.649	4.00	112.6	163.4	231.6	0.039	0.088	16.631	0.017	-0.065
0.344	1.735	4.713	4.110	1.869	0.603	2.425	5.00	161.2	311.9	415.0	0.048	0.110	15.225	0.032	-0.063
0.412	2.519	4.771	3.964	2.238	0.807	2.593	5.99	247.3	525.0	762.3	0.058	0.132	16.278	0.058	-0.062
0.481	3.314	4.604	3.844	2.613	0.760	2.515	7.00	326.9	821.1	1176.5	0.067	0.154	15.787	0.091	-0.061
0.550	4.235	4.500	3.745	2.988	0.755	2.485	8.00	422.3	1209.6	1738.1	0.077	0.176	15.600	0.127	-0.060
0.619	5.343	4.482	3.660	3.363	0.822	2.529	9.00	544.4	1702.2	2521.8	0.087	0.198	15.878	0.167	-0.060
0.687	6.598	4.493	3.588	3.732	0.905	2.593	9.99	687.6	2301.0	3535.1	0.096	0.220	16.281	0.209	-0.062
0.756	7.931	4.460	3.524	4.107	0.937	2.607	11.00	837.2	3035.0	4736.5	0.106	0.242	16.369	0.254	-0.064
0.825	9.323	4.403	3.466	4.482	0.936	2.592	12.00	991.0	3907.5	6118.1	0.116	0.264	16.271	0.304	-0.068
0.894	10.823	4.353	3.415	4.856	0.938	2.579	13.00	1157.9	4930.0	7746.7	0.125	0.286	16.190	0.359	-0.072
0.962	12.470	4.331	3.369	5.226	0.962	2.591	13.99	1346.9	6095.4	9696.2	0.135	0.308	16.264	0.422	-0.078
0.997	13.382	4.327	3.347	5.416	0.980	2.603	14.50	1453.4	6759.8	10843.6	0.140	0.319	16.339	0.457	-0.082
1.031	14.342	4.337	3.327	5.601	1.010	2.627	15.00	1568.9	7449.0	12104.7	0.144	0.330	16.494	0.493	-0.085
1.066	15.372	4.348	3.306	5.791	1.042	2.653	15.51	1693.6	8205.0	13510.4	0.149	0.341	16.655	0.533	-0.089
1.100	16.470	4.375	3.287	5.976	1.088	2.693	16.00	1831.0	8986.0	15072.1	0.154	0.352	16.910	0.574	-0.093
1.169	18.940	4.455	3.251	6.350	1.204	2.799	17.00	2149.1	10717.3	18800.6	0.164	0.374	17.574	0.665	-0.102
1.237	21.969	4.615	3.218	6.720	1.397	2.983	17.99	2564.4	12624.4	23737.8	0.173	0.396	18.728	0.765	-0.111
1.306	26.028	4.905	3.187	7.095	1.718	3.295	19.00	3157.8	14774.2	30862.0	0.183	0.418	20.689	0.871	-0.121
1.375	31.723	5.393	3.158	7.469	2.235	3.805	20.00	4041.3	17151.0	41582.9	0.193	0.440	23.887	0.982	-0.131
1.444	39.213	6.045	3.131	7.844	2.914	4.476	21.01	5243.1	19765.5	56656.4	0.202	0.462	28.099	1.092	-0.141
1.512	46.870	6.590	3.105	8.214	3.485	5.039	21.99	6471.8	22585.3	73226.8	0.212	0.484	31.635	1.194	-0.149

18/07/2024 18:11

Ship Model No:2641- Test No:002

Resistance test results

Scale ratio	λ	56.00	
Temperature of sea water (std)	t_s	15.00	°C
Temperature of tank water	t_m	22.00	°C
Viscosity of sea water (std)	ν_s	1.1892	$*10^{-6}$ m²/s
Viscosity of tank water	ν_m	0.9565	$*10^{-6}$ m²/s
Mass density of sea water	ρ_s	1026.021	Kg/m³
Mass density of tank water	ρ_m	997.774	Kg/m³
Incremental resistance coefficient	Δc	2.000	$*10^{-4}$
Form Factor	$1+k$	1.000	

Length between perpendiculars	L_{pp}	280.000	m
Length of waterline	L_{WL}	278.281	m
Length overall submerged	L_{OS}	278.281	m
Breadth moulded max	B_M	45.000	m
Breadth of waterline	B_{WL}	45.000	m
Draft at forward perpendicular	T_F	7.215	m
Draft at afterward perpendicular	T_A	10.015	m
Draft at midship	T_M	8.615	m
Displacement weight	Δ	89185	t
Area of wetted surface	S_S	14668.30	m²
Block coefficient	C_B	0.8065	

V_m m/s	RT_m N	CT_m $*10^3$	CF_m $*10^3$	RN_m $*10^{-6}$	CR $*10^3$	CT_s $*10^3$	V_s Knots	RT_s kN	PEF kW	PE kW	F_n	$F_{n\nabla}$	CT_∇	DTF m	DTA m
0.275	0.804	4.566	4.344	1.429	0.222	2.101	4.00	67.0	123.2	137.8	0.039	0.099	15.708	0.014	0.009
0.344	1.274	4.627	4.149	1.786	0.478	2.310	5.00	115.0	234.5	295.7	0.049	0.123	17.267	0.015	0.009
0.412	1.804	4.545	3.998	2.143	0.547	2.341	6.00	167.9	397.2	518.3	0.059	0.148	17.502	0.018	0.012
0.481	2.402	4.451	3.878	2.500	0.573	2.337	7.00	228.0	619.7	821.0	0.069	0.173	17.466	0.024	0.015
0.550	3.088	4.378	3.777	2.857	0.600	2.338	8.00	298.0	911.7	1226.7	0.079	0.198	17.477	0.033	0.020
0.619	3.872	4.336	3.692	3.214	0.644	2.360	9.00	380.6	1281.2	1762.3	0.089	0.222	17.639	0.045	0.027
0.688	4.764	4.324	3.618	3.572	0.706	2.402	10.00	478.4	1737.9	2461.4	0.099	0.247	17.955	0.060	0.035
0.756	5.784	4.338	3.553	3.929	0.784	2.463	11.00	593.5	2289.0	3358.4	0.108	0.272	18.410	0.078	0.044
0.825	6.941	4.368	3.496	4.286	0.872	2.536	12.00	727.1	2943.8	4488.1	0.118	0.296	18.954	0.100	0.055
0.894	8.215	4.406	3.444	4.643	0.962	2.611	13.00	878.8	3711.7	5877.3	0.128	0.321	19.518	0.127	0.067
0.962	9.607	4.446	3.397	5.000	1.050	2.686	14.00	1048.3	4599.0	7549.9	0.138	0.346	20.077	0.157	0.081
0.997	10.352	4.467	3.375	5.179	1.092	2.722	14.50	1139.9	5091.1	8502.7	0.143	0.358	20.350	0.174	0.088
1.031	11.137	4.489	3.354	5.357	1.135	2.759	15.00	1236.5	5616.6	9541.7	0.148	0.370	20.627	0.191	0.096
1.066	11.960	4.514	3.334	5.536	1.180	2.799	15.50	1339.2	6176.3	10679.3	0.153	0.383	20.921	0.210	0.104
1.100	12.823	4.544	3.314	5.714	1.230	2.843	16.00	1449.3	6769.7	11929.2	0.158	0.395	21.251	0.230	0.112
1.169	14.744	4.627	3.278	6.072	1.349	2.952	17.00	1699.2	8070.0	14860.5	0.167	0.420	22.068	0.274	0.131
1.237	17.019	4.763	3.244	6.429	1.519	3.113	18.00	2008.4	9521.8	18597.1	0.177	0.444	23.267	0.323	0.150
1.306	19.812	4.975	3.213	6.786	1.763	3.347	19.00	2406.7	11137.5	23525.1	0.187	0.469	25.023	0.377	0.171
1.375	23.293	5.279	3.183	7.143	2.096	3.672	20.00	2925.4	12920.6	30099.3	0.197	0.494	27.452	0.436	0.193
1.444	27.528	5.661	3.156	7.500	2.505	4.074	21.00	3577.9	14884.2	38654.2	0.207	0.518	30.451	0.501	0.217
1.512	32.341	6.060	3.130	7.857	2.930	4.491	22.00	4329.0	17030.6	48994.5	0.217	0.543	33.572	0.571	0.243

18/07/2024 18:20

Figure 27: Test data of the two series of the JBC model

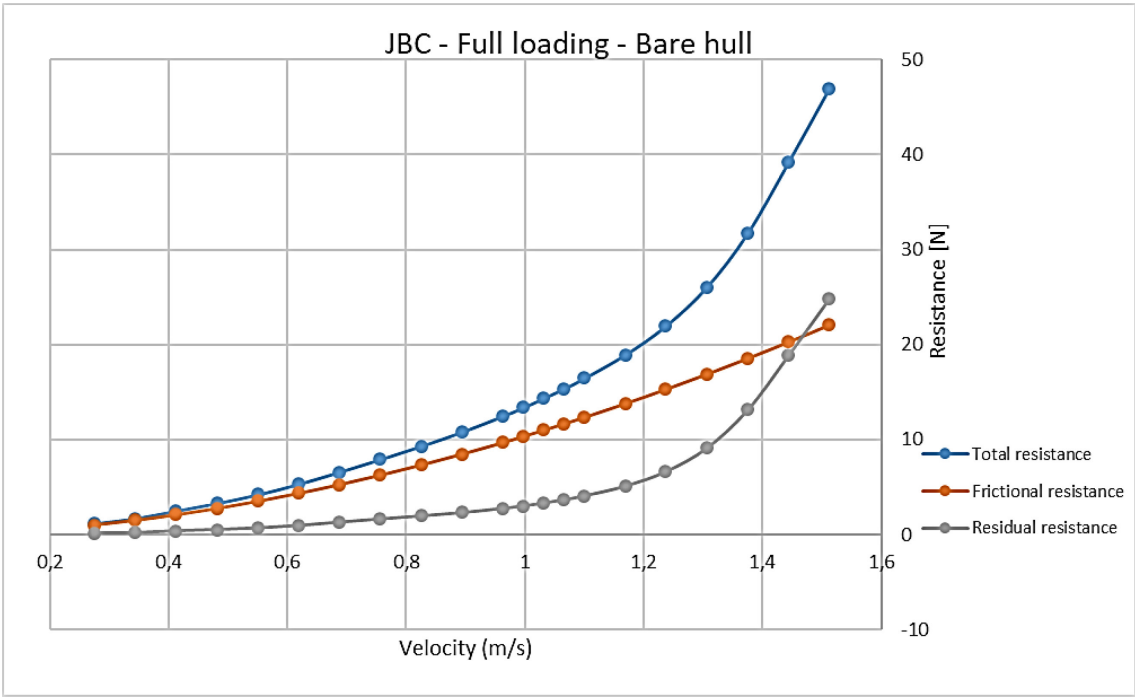
JBC - Full loading - Bare hull
50
40
30
20
10
0
-10
Resistance [N]
0,2
0,4
0,6
0,8
1
1,2
1,4
1,6
Velocity (m/s)
Total resistance
Frictional resistance
Residual resistance

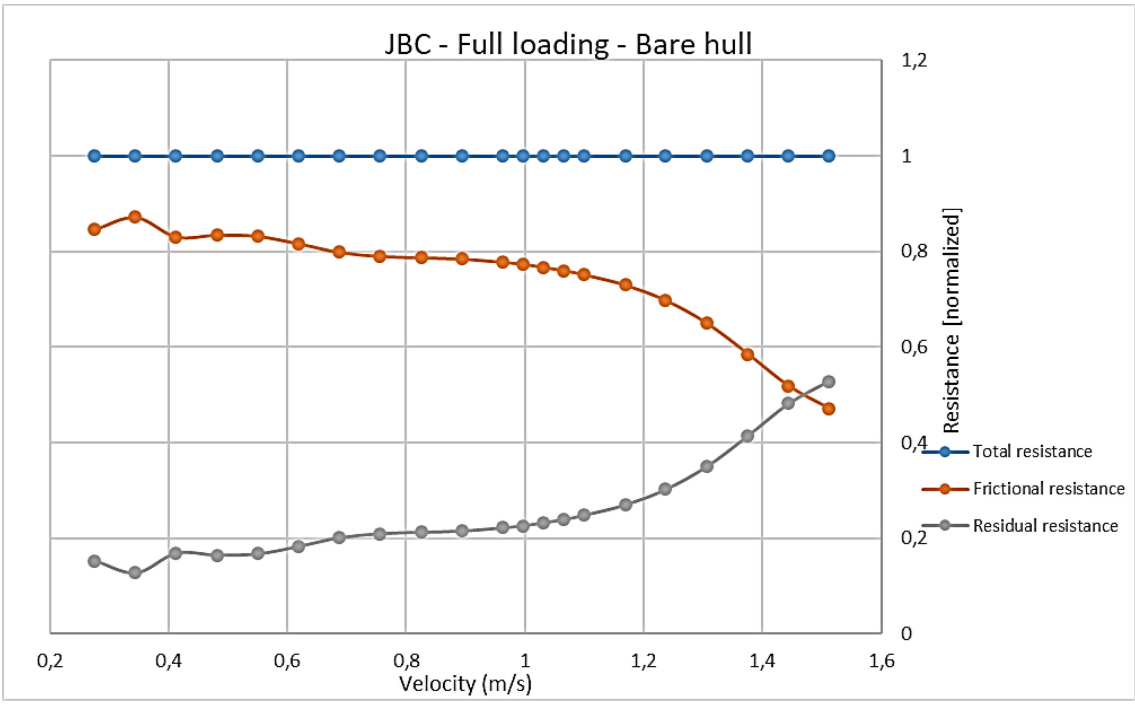
JBC - Full loading - Bare hull
1,2
1
0,8
0,6
0,4
0,2
0
Resistance [normalized]
0,2
0,4
0,6
0,8
1
1,2
1,4
1,6
Velocity (m/s)
Total resistance
Frictional resistance
Residual resistance

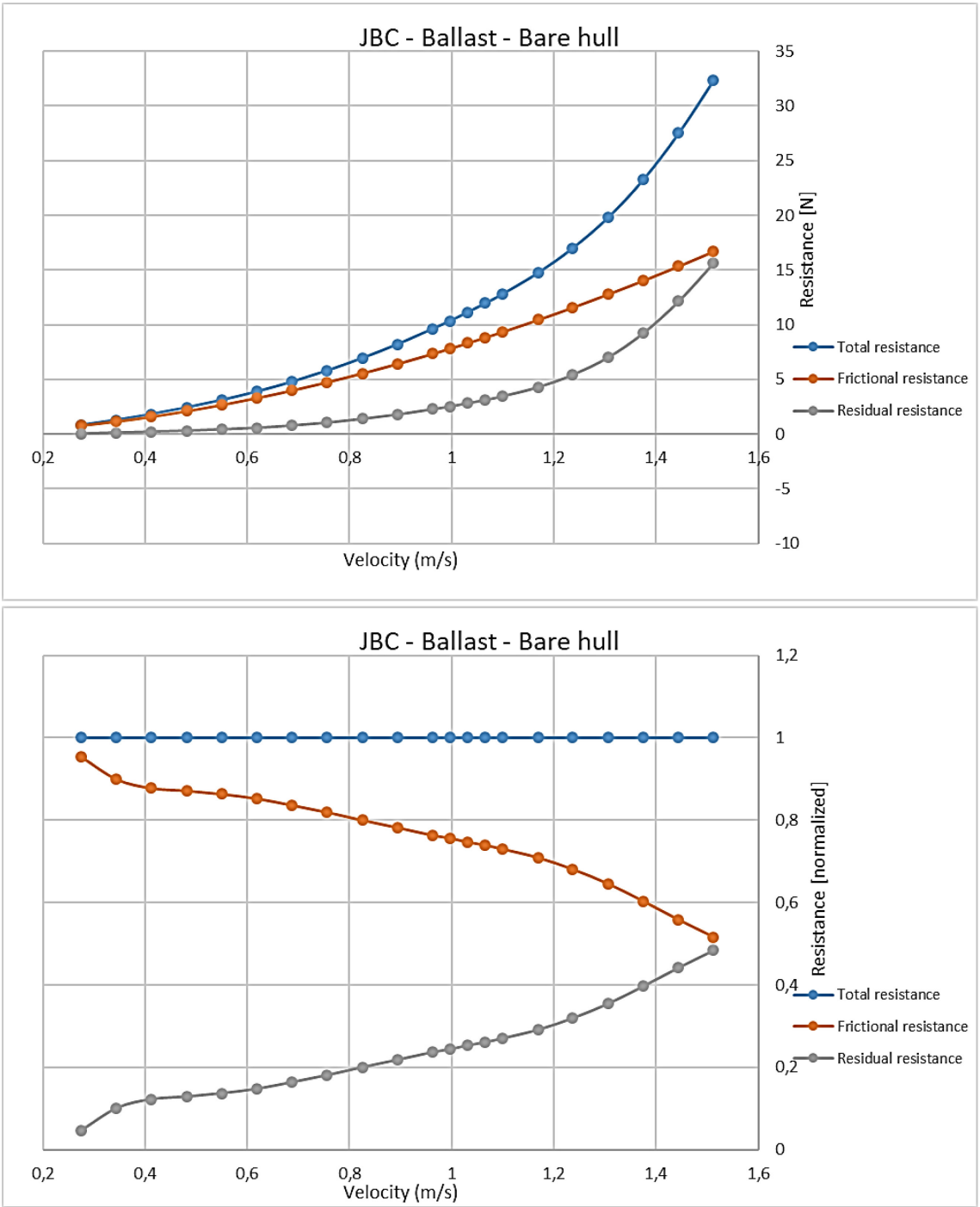

Figure 28: Graphical results for the JBC model

The results for the JBC model reflect a good and standard naval design with a classical inversion of the frictional and residual resistance at high speed. While at low speed, and anyway in the operative range of ship, the frictional resistance is the largest portion of the whole resistance (both at full and ballast loading condition, the frictional resistance is more than 70% of the total resistance), starting from 16 knots, the residual resistance starts to increase rapidly and the two equals each other at the highest investigated speed. In full load condition, at 22 knots, the residual resistance is even higher

than the frictional one. This behaviour is quite standard considering the kind of ship that generally present a well-defined operative range. The increase of the residual resistance appears to be more pronounced in full loading condition, anyway in the operative range (likely, 12-17 knots) the C_T in full loading condition is lower than the one in ballast loading condition (Figure 28).

9 Conclusions

This deliverable has conducted a comprehensive review of the design and application of Passive Air Lubrication Systems (PALS) for ships, with a particular focus on their potential to enhance ship efficiency and reduce environmental impact. The report provides valuable insights into the optimisation of system performance through a detailed analysis of PALS operating principles, key variables influencing drag reduction and parametric testing methods. It highlights key factors influencing PALS performance, including the air injection rate, the air-water volume fraction and the hydrostatic pressure.

The study acknowledges the increasing importance of regulations aimed at curbing maritime emissions and highlights the role of PALS as a viable solution for ship operators seeking to comply with these regulations.

The focus of this deliverable are the design and implementation of the PALS system to be installed as a proof of concept in two scaled hull models, which will be tested in the CNR-INM towing tank. The report examines various design considerations, especially focusing on the injector shape optimisation and arrangement (placement) beneath the hulls, to ensure optimal system operation.

The design of the rig which generates an air-water mixture to be injected beneath the hull to form the air-bubble carpet is detailed. The mixture is generated through venture tubes. Pressures and flow rates are controlled using a series of feedback control valves with associated flowmeters.

The experimental measurement setup and the results of baseline tests, i.e. performed on the two hulls without the PALS in operation, are also detailed.

References

[1] ZEWT, “Executive Summary Realizing zero-emission,” 2023.
[2] Sindagi, S., Vijayakumar, R., Nirali, S., Saxena, B.K., "Numerical Investigation of Influence of Microbubble Injection, Distribution, Void Fraction and Flow Speed on Frictional Drag Reduction" in Murali, K., Sriram, V., Samad, A., Saha, N. (eds) *Proceedings of the Fourth International Conference in Ocean Engineering* (ICOE2018). *Lecture Notes in Civil Engineering*, vol 22. Springer, Singapore, 2019, Doi:10.1007/978-981-13-3119-0_17.
[3] Hassan, Y. A., Gutierrez-Torres, C.C., “Investigation of drag reduction mechanism by microbubble injection within a channel boundary layer using particle tracking velocimetry” *Nucl. Eng. Technol.*, vol. 38, 763–778, 2006.
[4] Verschoof, R.A., van der Veen, R.C.A., Sun, C., Lohse, D., " Bubble Drag Reduction Requires Large Bubbles", Phys. Rev. Lett., vol. 117, 104502, 2016, Doi: 10.1103/PhysRevLett.117.104502.
[5] Xu, J., Maxey, M., Karniadakis, G.E., " Numerical simulation of turbulent drag reduction using micro-bubbles", *J. Fluid Mech.*, vol. 468, 271-281, 2002, Doi: 10.1017/S0022112002001659.
[6] Gao, Q., Lu, J., Zhang, G., Zhang, J., Wu, W., Deng, J., “Experimental study on bubble drag reduction by the turbulence suppression in bubble flow” *Ocean Eng.*, vol. 272, 113804, 2023, Doi: 10.1016/j.oceaneng.2023.113804.
[7] Stephani, K.A., Marr, K.C., Doctor, R., Goldstein, D.B., “Drag Reduction using Trapped Bubbles on a Flat Plate Surface” in *3rd AIAA Flow Control Conference, San Francisco (CA)* 2006, Doi: 10.2514/6.2006-3193.
[8] Gutierrez-Torres, C.C., Hassan, Y., Jiménez Bernal, J., Barbosa Saldaña, J., “Drag reduction by microbubble injection in a channel flow”, *Rev. Mex. Fís.*, vol. 54, 8–14, 2008.
[9] Jiménez, J., Pinelli, A., “The autonomous cycle of near-wall turbulence,” *J. Fluid Mech.*, vol. 389, 335–359, 1999, Doi: 10.1017/S0022112099005066.
[10] Jacob, B., Olivieri, A., Miozzi, M., Campana, E.F., Piva, R., “Drag reduction by microbubbles in a turbulent boundary layer Drag reduction by microbubbles in a turbulent boundary layer” *Phys. Fluids,* vol. 22, 115104, 2010, Doi: 10.1063/1.3492463.
[11] Sanders, W.C., Winkel, E.S., Dowling, D.R., Perlin, M., Ceccio, S.L., “Bubble friction drag reduction in a high-Reynolds-number flat-plate turbulent boundary layer,” *J. Fluid Mech.*, vol. 552, 353–380, 2006, Doi: 10.1017/S0022112006008688.
[12] Murai, Y., “Frictional drag reduction by bubble injection” *Exp. Fluids*, vol. 55, 1773, 2014, Doi: 10.1007/s00348-014-1773-x.
[13] Elbing, B.R., Winkel, E.S., Lay, K.A., Ceccio, S.L., Dowling, D.R., Perlin, M., “Bubble-induced skin-friction drag reduction and the abrupt transition to air-layer drag reduction” *J. Fluid Mech.*, vol. 612, 201–236, 2008, Doi: 10.1017/S0022112008003029.
[14] Kawamura, T., Moriguchi, Y., Kato, H., Kakugawa, A., Kodama, Y., “Effect of bubble size on the microbubble drag reduction of a turbulent boundary layer,” *Proc. ASME/JSME Jt. Fluids Eng. Conf.*, vol. 2 A, 647–654, 2003, Doi: 10.1115/fedsm2003-45645.
[15] Pavlov, G.A., Yun, L., Bliault, A., He, S-L. *Air Lubricated and Air Cavity Ships*. 2020. Doi: 10.1007/978-1-0716-0425-0.
[16] Sindagi, S., Vijayakumar, R., Saxena, B.K., "Investigation of air lubrication system (ALS) on drag reduction of ship", *6th Worldwide Maritime Technology Conference* (WMTC - 18), Shanghai, CN, 2019.
[17] Kodama, Y., Kakugawa, A., Takahashi, T., Nagaya, S., Sugiyama, K., “Microbubbles: drag reduction mechanism and applicability to ships,” in *24th Symp. Naval Hydrodynamics*, 2002, 1–19.
[18] Harleman, M.J.W., “On the effect of turbulence on bubbles: experiments and numercal simulations of bubbles in wall-bounded flows.” *Ph.D. Thesis*, TU Delft, The

Netherlands, 2012.
[19] Jang, J., Choi, S.H., Ahn, S., Kim, B., Seo, J.S., "Experimental investigation of frictional resistance reduction with air layer on the hull bottom of a ship," *Int. J. Nav. Archit. Ocean Eng.*, vol. 6, 363–379, 2014, Doi: 10.2478/IJNAOE-2013-0185.
[20] Foeth, E.J., Eggers, R., van der Hout, I., Quadvlieg, F.H.H.A., "Reduction of frictional resistance by air bubble lubrication" SNAME Maritime Convention, Providence, Rhode Island, USA, 2009, Doi: https://doi.org/10.5957/SMC-2009-009
[21] Kunz, R.F., Gibeling, H.J., Maxey, M.R., Tryggvason, G., Fontaine, A.A., Petrie, H.L., Ceccio, S.L., "Validation of Two-Fluid Eulerian CFD Modeling for Microbubble Drag Reduction Across a Wide Range of Reynolds Numbers" *J. Fluids Eng.*, vol. 129, 66-79, 2007, Doi: 10.1115/1.2375124.
[22] Jha, N.K., Bhatt, A., Govardhan, R.N., "Effect of bubble distribution on wall drag in turbulent channel flow" *Exp. Fluids*, vol. 60, 127, 2019, Doi: 10.1007/s00348-019-2773-7.
[23] Feng, Y.Y., Hu, H., Peng, G.Y., Zhou, Y., "Microbubble effect on friction drag reduction in a turbulent boundary layer" *Ocean Eng.*, vol. 211, 107583, 2020, Doi: 10.1016/j.oceaneng.2020.107583.
[24] Mohanarangam, K., Cheung, S.C.P., Tu, J.Y., Chen, L., "Numerical simulation of micro-bubble drag reduction using population balance model" *Ocean Eng.*, vol. 36, 863–872, 2009, Doi: 10.1016/j.oceaneng.2009.05.001.
[25] Tanaka, T., Oishi, Y., Park, H.J., Tasaka, Y., Murai, Y., Kawakita, C., "Frictional drag reduction caused by bubble injection in a turbulent boundary layer beneath a 36-m-long flat-bottom model ship" *Ocean Eng.*, vol. 252, 111224, 2022, Doi: 10.1016/j.oceaneng.2022.111224.
[26] Kanai, A., Miyata, H., "Direct numerical simulation of wall turbulent flows with microbubbles" *Int. J. Meth Fluids*, vol. 35, 593–615 , 2001, Doi: https://doi.org/10.1002/1097-0363(20010315)35:5<593::AID-FLD105>3.0.CO;2-U.
[27] Meng, J.C.S., Uhlman, J.S., "Microbubble formulation and splitting in a turbulent boundary layer for turbulence reduction" *Advances in Fluids Dynamics*, 1989, Doi: 10.1007/978-1-4612-3684-9_14.
[28] Deutsch, S, Moeny, M., Fontaine, A., Petrie, H., "Microbubble drag reduction in rough walled turbulent boundary layers" in *Proceedings of the ASME Fluid Engng Division Summer Meeting, FEDSM2003-45647,* 665-673, 2003, Doi: 10.1115/FEDSM2003-45647
[29] Kodama, Y., Kakugawa, A., Takahashi, T., Kawashima, H., "Experimental study on microbubbles and their applicability to ships for skin friction reduction" *Int. J. Heat Fluid Flow*, vol. 21, 582–588, 2000, Doi: 10.1016/S0142-727X(00)00048-5.
[30] Sayyaadi, H., Nematollahi, M., "Determination of optimum injection flow rate to achieve maximum micro bubble drag reduction in ships; An experimental approach" *Sci. Iran.*, vol. 20, 535–541, 2013, Doi: 10.1016/j.scient.2013.05.001.
[31] Tsai, J.-F.. Chen, C-C, "Boundary Layer Mixture Model for a Microbubble Drag Reduction Technique," *Int. Schol. Res. Network, ISRN Mech. Eng.*, vol. 2011, 405701, 2011, Doi: 10.5402/2011/405701.

[32] Wu, S.-J., Ouyang, K., Shiah, S.-W., “Robust design of microbubble drag reduction in a channel flow using the Taguchi method” *Ocean Eng.*, vol. 35, 856–863, 2008, Doi: 10.1016/j.oceaneng.2008.01.022.
[33] Latorre, R., “Ship hull drag reduction using bottom air injection” *Ocean Eng.*, vol. 24, 161–175, 1997, Doi: 10.1016/0029-8018(96)00005-4.
[34] Ceccio, S.L., Perlin, M., Elbing, B.R., “A cost-benefit analysis for air layer drag reduction” *Int. Conf. Ship Drag Reduction*, 2010.
[35] Harries, S., "Practical shape optimization using CFD: state-Of-The-Art in industry and selected trends", in *Conference on computer applications and information technology in the maritime industries* (COMPIT), Pontignano, Italy, 2020.
[36] Renzsch, H., Meyer, J., Graf, K., "Investigation of Modern Sailing Yachts Using a New Free-Surface RANSE Code", *International Conference on Innovation in High Performance Sailing Yachts*, Lorient, FR, 2017.
[37] Meyer, J., Renzsch, H., Graf, K., Slawig, T., "Advanced CFD-Simulations of free-surface flows around modern sailing yachts using a newly developed OpenFOAM solver", *The 22nd Chesapeake Sailing Yacht Symposium*, Annapolis, MD, USA, 2016.
[38] Patankar, S.V., Spalding, D.B., "A calculation procedure for heat, mass and momentum transfer in three-dimensional parabolic flows", Int. J. Heat Mass Transfer, Vol. 15, 1787–1906 , 1972, Doi: 10.1016/0017-9310(72)90054-3.
[39] Issa, R.I., "Solution of the Implicitly Discretized Fluid Flow Equations by Operator-Splitting", *J. Comput. Phys*., vol. 62, 40-65, 1985, Doi: 10.1016/0021-9991(86)90099-9.
[40] Menter, F.R., Kuntz, M., Langtry, R., "Ten Years of Industrial Experience with the SST Turbulence Model", in *Turbulence, Heat and Mass Transfer 4*, eds: Hanjalic, K., Nagano, Y., Tummers, M.J., Begell House, Inc., 2003.
[41] Hirt, C.W., Nichols, B.D., "Volume of fluid (VOF) method for the dynamics of free boundaries", *J. Comput. Phys*., vol. 39, 201-225, 1981, Doi: 10.1016/0021-9991(81)90145-5.
[42] Wackers, J., Koren, B., Raven, H.C., van der Ploeg, A., Starke, A.R., Deng, G.B., Queutey, P., Visonneau, M., Hino, T., Ohashi, K., "Free-surface viscous flow solution methods for ship hydrodynamics", *Archives of Computational Methods in Engineering,* vol. 18, 1-41, 2011, Doi: 10.1007/s11831-011-9059-4.
[43] ITTC, “Resistance and Propulsion Test and Performance Prediction with Skin Frictional Drag Reduction Techniques” *ITTC Qual. Syst. Man. Recomm. Proced. Guidelines,* 2017.